PÁLFY, J. & ZAJZON, N. 2012. Environmental changes across the Triassic-Jurassic boundary and coeval volcanism inferred from elemental geochemistry and mineralogy in the Kendlbachgraben section (Northern Calcareous Alps, Austria). *Earth and Planetary Science Letters* **335-336**: 121–134.

MTA–MTM–ELTE Paleo contribution number: 167.

1   **Environmental changes across the Triassic-Jurassic boundary and coeval**

2   **volcanism inferred from elemental geochemistry and mineralogy in the**

3   **Kendlbachgraben section (Northern Calcareous Alps, Austria)**

4

5   József Pálfy[a, b, *], Norbert Zajzon[c]

6

7   [a] Department of Physical and Applied Geology, Eötvös Loránd University, Pázmány P. sétány

8   1/C, Budapest, H-1117 Hungary; e-mail: palfy@nhmus.hu

9   [b] Research Group for Paleontology, Hungarian Academy of Sciences–Hungarian Natural

10   History Museum– Eötvös Loránd University, POB 137, Budapest, H-1431 Hungary

11   [c] Institute of Mineralogy and Geology, University of Miskolc, Miskolc-Egyetemváros, H-

12   3515 Hungary; e-mail: nzajzon@uni-miskolc.hu

13   [*] Corresponding author. Telephone: +36 1 372 2500 ext. 8728; Fax: +36 1 381 2130

14

15 **Environmental changes across the Triassic-Jurassic boundary and coeval**

16 **volcanism inferred from elemental geochemistry and mineralogy in the**

17 **Kendlbachgraben section (Northern Calcareous Alps, Austria)**

18

19 József Pálfy, Norbert Zajzon

20

21 **Abstract**

22 　　The end-Triassic extinction (ETE), one of the five largest Phanerozoic mass extinctions,

23 is associated with rapid and severe environmental change, but existing data permit alternative

24 models of causation. Volcanism in the Central Atlantic Magmatic Province (CAMP) has been

25 proposed as the main trigger, but direct evidence for this linkage is scarce. To help constrain

26 scenarios for the ETE and other Triassic-Jurassic boundary (TJB) events, we obtained a

27 temporally highly resolved, multidisciplinary dataset from the Kendlbachgraben section in the

28 Northern Calcareous Alps in Austria. The section belongs to the same paleogeographic unit

29 (Eiberg Basin) and share similar stratigraphy with the recently selected base Jurassic Global

30 Stratotype Section and Point at Kuhjoch.

31 　　Micromineralogic study of the topmost bed of the Rhaetian Kössen Formation revealed

32 pseudomorphs of altered, euhedral pyroxene and amphibole crystals. Their well-faceted

33 morphology is consistent with their origin from distal mafic volcanic ash fallout. Spherical

34 grains were also observed in the same bed, likely representing clay-altered volcanic glass.

35 Clay minerals of this bed include low- to medium-charged smectite and Mg-vermiculite, both

36 typical alteration products of mafic rocks. The same bed yielded a rare earth element pattern

37 that differs from all other levels in an enrichment of heavy REEs, hinting at some minor

38 contribution from mafic magmatic material. These features from a layer that was deposited

39 very near to the TJB are interpreted as direct evidence of CAMP volcanism, coeval or

40 immediately preceding the ETE and the initial negative carbon isotope anomaly.

41   The kaolinite-dominated clay mineral spectrum of the overlying boundary mudstone

42 records intensive weathering under hot and humid greenhouse conditions. Redox-sensitive

43 minor and trace elements do not support the development of widespread anoxia in the studied

44 section. Although pyrite is common in several layers, framboid size indicates formation

45 within a reductive zone, below the sediment/water interface, rather than in an anoxic water

46 column.

47   Our data provide a direct link between uppermost Triassic marine strata and CAMP-

48 derived material. They support scenarios where CAMP volcanism induced climate and other

49 environmental change, which in turn triggered the ETE and that is also reflected in the carbon

50 isotope anomalies.

51

52

53 **Keywords:** Triassic-Jurassic boundary; end-Triassic extinction; Northern Calcareous Alps;

54 micromineralogy; rare earth elements; redox-sensitive elements

55

56

57 **1. Introduction**

58   The Triassic-Jurassic boundary (TJB) is preceded by one of the five largest Phanerozoic

59 biotic crises, the end-Triassic extinction (ETE) (Alroy, 2008; Raup and Sepkoski, 1982),

60 which in turn was associated with and likely triggered by rapid and severe environmental

61 change (Hesselbo et al., 2007). The biotic change is manifest in a pronounced loss of global

62 diversity (Sepkoski, 1981, 1993), major turnover in several marine and terrestrial groups

63 (Carter and Hori, 2005; Flügel, 2002; Kiessling et al., 2007; McElwain and Punyasena, 2007;

64 Olsen et al., 1987) and ecologic reorganization (McElwain et al., 2007; McGhee et al., 2004).

65 A major perturbation of the global carbon cycle likely reflects environmental disturbances and

66 is recorded by carbon isotope anomalies in the TJB interval, documented at numerous

67 localities worldwide (Galli et al., 2007; Guex et al., 2004; Hesselbo et al., 2002; Pálfy et al.,

68 2001; Ruhl et al., 2009; Ward et al., 2001). Volcanism in the Central Atlantic Magmatic

69 Province (CAMP) has been proposed to be synchronous with and therefore considered as the

70 trigger for concomitant environmental and biotic change (Marzoli et al., 1999, 2004; Pálfy,

71 2003). The ETE and TJB events have been in the focus of much recent research effort, yet

72 several questions about the trajectory and causal chain of events remain open to debate

73 (Hesselbo et al., 2007). Significantly, the key role of CAMP volcanism in triggering the

74 extinction has been doubted (Whiteside et al., 2007) and alternative scenarios invoking a

75 putative extraterrestrial impact event (Olsen et al., 2002), rapid sea level changes (Hallam and

76 Wignall, 1999) or widespread marine anoxia (Hallam, 1995) have been proposed. Other

77 possible proximate causes of the extinction include climate change, notably extreme

78 greenhouse warming (McElwain et al., 1999; Schaller et al. 2011; Steinthorsdottir et al. 2011)

79 and a marine biocalcification crisis (Hautmann, 2004; Hautmann et al., 2008). To further test

80 these competing models of the TJB events, we obtained a temporally highly resolved,

81 multidisciplinary dataset from the Kendlbachgraben section in Austria.

82   The Northern Calcareous Alps is a classical area of TJB studies and the section at

83 Kendlbachgraben is the one with longest history of research (Golebiowski and Braunstein,

84 1988; Hallam, 1990; Suess and Mojsisovics, 1868). The search for a Global Stratotype

85 Section and Point (GSSP) for the system boundary generated much renewed interest in the

86 TJB in general, and in the Austrian sections in particular. The newly selected base Jurassic

87 GSSP at Kuhjoch (Hillebrandt et al., 2007) and the Kendlbachgraben section are both located

88 within the Eiberg Basin (Fig. 1), now separated by 130 km, and share similar stratigraphies.

89   Thus our results reported herein have both regional and global relevance in constraining

90   models for the ETE and TJB events.

91   The Kendlbachgraben section preserves a marine succession across the TJB which,

92   together with the other well-correlated sections in the Eiberg Basin (Fig. 2), provide an

93   excellent record of both the biotic turnover in various fossil groups and the significant

94   changes in sedimentation (Golebiowski, 1990; Krystyn et al., 2005). The evolution of carbon

95   isotope composition yielded a useful proxy record of environmental change (Ruhl et al.,

96   2009).

97   Here we further explore the geochemistry and mineralogy of this section, in order to

98   answer some of the remaining questions about the ETE and TJB events. Key issues addressed

99   in this contribution concern climate change around the TJB in the source area of terrigenous

100   sediment input, the redox conditions of local sedimentary environments, and detection of any

101   volcanically-derived material in the section that might allow direct correlation with CAMP

102   volcanic activity. Changes in humidity are inferred from major element chemistry reflecting

103   detrital input, variations in clay mineralogy and enrichment in immature terrigenous

104   components. Development of oxygen deficient conditions is tracked on the basis of redox-

105   sensitive trace elements and distribution of pyrite. Clues of contemporaneous volcanism are

106   sought in the rare earth elements (REE) abundance patterns and the micromineralogical

107   spectrum.

108

109   **2. Geological setting**

110   The Kendlbachgraben section is located about 30 km southeast of Salzburg and 8 km

111   southwest of Wolfgangsee in the Osterhorn Range in Salzkammergut, Austria. Access is via a

112   forest road in the Zinkenbach valley. The studied section is exposed on the steep hillside

113   immediately above the forest road (coordinates 47° 41' 21"N, 13° 21' 37"E), only ~300 m NW

114 from the point where the road crosses the gully which exposes the classical, long-known

115 Kendlbachgraben section. The stratigraphic significance of this locality for the Triassic-

116 Jurassic boundary was first recognized by Suess and Mojsisovics (1868). Modern studies

117 focussed on palynostratigraphy (Morbey, 1975), changes in facies and macrofauna

118 (Golebiowski and Braunstein 1988; Golebiowski 1990), and carbon isotope stratigraphy

119 (Hallam and Goodfellow, 1990; Morante and Hallam, 1996; Ruhl et al., 2009).

120   The Kendlbachgraben section is located within the Eiberg Basin, an elongated, Late

121 Triassic–Early Jurassic intraplatform basin on the shelf of the western Neotethys. Correlative,

122 stratigraphically closely similar, and well studied sections elsewhere in the presently east-west

123 trending, 200 km long and 20 km wide Eiberg Basin include the nearby Tiefengraben

124 (Kürschner et al., 2007), the base Jurassic GSSP at Kuhjoch (Fig. 2) and its sister section at

125 Hochalplgraben (Hillebrandt et al., 2007; Hillebrandt and Krystyn, 2009; Bonis et al., 2009).

126 The Kendlbachgraben section is situated in the eastern segment of the Eiberg Basin,

127 structurally within the Osterhorn syncline, which in turn belongs to the Stauffen-

128 Höllengebirge nappe of the northern Tirolicum unit of the Northern Calcareous Alps (Linzer

129 et al., 1995). The Kuhjoch GSSP locality is located in the western Eiberg basin, now

130 preserved within the Karwendel syncline. Both sections are thought to represent proximal

131 basin facies, sandwiched between the extensive Dachstein platform and its platform margin

132 reefs (preserved as the "Oberrhätkalk") (Krystyn et al., 2005).

133   At Kendlbachgraben, the base of the section is represented by the uppermost Triassic

134 Eiberg Member of the Kössen Formation, a dark colored, pure limestone of bioclastic

135 wackestone texture. Our XRD measurements reveal a 98–99% calcite content, and only the

136 remaining 1–2% is of detrital and organic origin. The topmost Rhaetian conodont *Misikella*

137 *posthernsteini* is reported from the highest limestone bed (Golebiowski and Braunstein,

138 1988).

139   The transition at the formation boundary is represented by a 5 cm thick marlstone

140   layer, overlain by 5 cm of brown claystone, yielding bivalves (e.g. *Cardinia, Chlamys*)

141   (Golebiowski and Braunstein, 1988) and fish scales. The initial negative carbon isotope

142   anomaly was detected at this level (Ruhl et al., 2009). The basal part of the overlying

143   Kendlbach Formation is the ~2.5 m thick clay-rich boundary mudstone ("Grenzmergel" in the

144   traditional terminology) which forms the basal part of the Tiefengraben Member. Early claims

145   of a broad negative carbon isotope anomaly in this unit (Hallam and Goodfellow, 1990) were

146   withdrawn on the basis of diagenetic overprint (Morante and Hallam, 1996). Higher upsection

147   the Tiefengraben Member is composed of intercalated beds of marl and impure limestone, in

148   turn overlain by the carbonate-dominated Breitenberg Member. Stable carbon isotope

149   stratigraphy, in agreement with lithostratigraphy, permits good correlation with the GSSP

150   section at Kuhjoch and suggests placement of the TJB in the middle of the Tiefengraben

151   Member, where the main negative carbon isotope anomaly starts at ~3 m above the formation

152   boundary (Ruhl et al., 2009).

153

154   **3. Material and methods**

155   A suite of 59 samples was collected from the section for whole rock major- and trace

156   element analyses. The topmost layer of the Kössen Formation was sampled in duplicate

157   (KBL-0 and KB-1) at different times and analyzed in different batches. Samples KB-2 and

158   KB-3 originate from the first two layers immediately overlying the Kössen Formation,

159   whereas 11 closely spaced samples represent the "Grenzmergel", the boundary mudstone.

160   One sample was taken from each of the 5 to 40 cm thick individual layers of the overlying 9.5

161   m of alternating shale-marlstone and limestone lithologies of the Kendlbach Formation,

162   except for the thickest (80 cm) marlstone interlayer which provided samples KB-31 and KB-

163   32. From this part of the section, a total of 30 samples are from limestone beds (sample

164   numbers prefixed KBL), whereas 28 samples are from shale or marlstone (prefixed KB). A

165   subset of selected samples was further subjected to mineralogical analyses.

166   Chemical analyses were carried out at the Acme Analytical Laboratories Ltd.,

167   Vancouver, Canada. Total abundance of major oxides and several minor elements (Si, Al, Fe,

168   Ca, Mg, Na, K, Mn, Ti, P, Cr) is reported on the basis of 0.2 g samples analyzed by

169   inductively-coupled plasma optical emission spectrometry (ICP-OES) following a lithium-

170   metaborate/tetraborate fusion and dilute nitric digestion. Loss on ignition (LOI) was

171   determined by weight difference after ignition at 1000°C. Total carbon and sulphur analysis

172   were done on a Leco instrument. Rare earth (La, Ce, Pr, Nd, Sm, Eu, Gd, Tb, Dy, Ho, Er, Tm,

173   Yb, Lu) and refractory elements (Ba, Be, Co, Cs, Gd, Hf, Nb, Rb, Sc, Sn, Sr, Ta, Th, U, V,

174   W, Y, Zr) were determined by inductively-coupled plasma mass spectrometry (ICP-MS)

175   following lithium-metaborate/tetraborate fusion and nitric acid digestion of a 0.2 g sample

176   (using the same decomposition as for major oxides). In addition, a separate 0.5 g split was

177   digested in aqua-regia and analysed by ICP-MS to report the precious (Ag, Au, Cu) and base

178   metals (As, Bi, Cd, Hg, Mo, Ni, Pb, Sb, Se, Tl, Zn).

179   From the analysed elements the following were under the detection limit (given in

180   parentheses): Ag (0.1 ppm), Au (0.5 ppb), Hg (0.1 ppm), Se (0.5 ppm) and Tl (0.1 ppm).

181   Concentrations of Be (1 ppm), Bi (0.1 ppm), Cd (0.1 ppm), Mn (100 ppm) and Sn (1 ppm)

182   were near their detection limit.

183   REE were normalized to the C1 chondrite (Anders and Grevesse, 1989). The cerium

184   anomaly was quantified using the following equation: $Ce/Ce^* = Ce_N/(La_N \cdot Pr_N)^{0.5}$, where

185   subscript N indicates the C1 chondrite normalized value (Anders and Grevesse, 1989). To

186   detect if any La enrichment occurred which may have caused an artefact in the Ce curve, we

187   calculated the Pr/Pr* ratios, where $Pr/Pr^* = Pr_N/(0.5^*Ce_N + 0.5^*Nd_N)$ (Bau and Dulski, 1996).

188   Scanning electron microscopy (both energy-dispersive spectroscopy (EDS) and

189   backscattered electron microscopy (BSE)) was carried out in polished sections from six

190   limestone samples, using a JEOL JXA-8600 Superprobe electron microscope (15 kV, 15 nA)

191   at the Institute of Mineralogy and Geology, University of Miskolc.

192   Micromineralogy studies focused on sample KB-1. After dissolving the carbonate with

193   5 wt% acetic acid, the >45 µm fraction was sieved and the grains were inspected and picked

194   under a stereo-microscope. To investigate the altered pyroxenes, amphiboles and clay

195   spherules of the sample, scanning electron microscopy and EDS measurements were done in

196   two laboratories. Secondary electron (SE) images were captured on a Hitachi S-4800 electron

197   microscope (20 kV, 10 µA) at BAY-NANO (Miskolc). EDS and BSE images were obtained

198   at the Department of Metallurgy, University of Miskolc, using an AMRAY-1860 T6

199   instrument (25 kV, 1–2 nA).

200   Whole rock mineral composition was determined and clay mineral investigations,

201   including X-ray powder diffraction (XRD) measurements were done at the Institute of

202   Mineralogy and Geology, University of Miskolc. The analyses were performed on a Bruker

203   D8 Advance X-ray powder diffractometer (Bragg-Brentano geometry, Cu tube at 40kV and

204   40mA, 2°–65° (2θ), 0.04° step scanning, 2 sec/step counting time, secondary graphite

205   monocromator, fixed slit system of 0.6 mm primary-, 0.6 mm secondary- and 0.2 mm

206   detector-slits, horizontal sample position, rotating sample holder), analyzed with EVA data

207   handling program of the Bruker Diffrac*Plus* evaluation software package, full profile fitting,

208   and a semi-quantitative method. Mineral species were identified based on the PDF2 (2005)

209   database, except for clay minerals. Semi-quantitative evaluation was performed only after the

210   identification of clay minerals by diagnostic procedures (Zajzon et al., in press).

211

212   **4. Results**

4.1. Major element geochemistry

Changes in the ratio of terrigenous siliciclastic components are traceable through the analysis of Si, Al and CO_3 (Table 1). The two dominant detrital phases are quartz and clay minerals. The sum of $SiO_2+Al_2O_3$ is taken to represent the quantity of the siliciclastics, whereas the amount of clay minerals is tracked by Al_2O_3. Changes in the ratio of clay minerals and detrital quartz are thus reflected in the SiO_2 vs. Al_2O_3 curve (Fig. 3).

Above the limestone beds of Kössen Formation, in the boundary mudstone, the detrital component increases abruptly and significantly, and reaches a maximum in sample KB-4. From here its amount gradually decreases upsection. The clay content is also highest in the boundary mudstone, and higher up quartz becomes more abundant among the detrital components.

The iron content is the lowest (0.07 wt% Fe_2O_3) in the pure limestones of the Kössen Formation. The other limestone interbeds higher in the section contain around 0.5 wt% Fe_2O_3. Much higher Fe content, typically between 3–4 wt%, is registered in the boundary mudstone (with peak values of 5.29 and 5.78 wt% in samples KB-4 and KB-8, respectively). The Jurassic marl interbeds usually contain 2–3 wt% Fe_2O_3.

The sulfur content in the section is low, except for the lower part of boundary mudstone and two other marl layers which contain more than 0.5 wt%. The sulfur content and partly also the iron in the samples is hosted by the pyrite and gypsum phases.

4.2. Redox-sensitive minor and trace elements

4.2.1. Redox-sensitive elements

The redox-sensitive elements such as Mo, Cd, V, U, Mn and other chalcophile elements (As, Sb, Sn and Cu) tend to concentrate in reducing environments in the form of sulphides or are absorbed in organic compounds (Berner, 1971; Calvert, 1976, Dolenec et al.,

10

238   2001). To filter out the dilution effect of the carbonate fraction on the signal, the measured

239   values were normalized to Th, which is regarded as an element of the terrigenous component

240   not controlled by the redox state of the depositional environment. Concentration of the redox-

241   sensitive elements remain low throughout the section (Table 1, Fig. 4). Enrichment in these

242   elements occurs only in the lowermost 10 cm of the boundary mudstone (samples KB-1, 2

243   and 3).

244

245   *4.2.2. U/Th ratio*

246   Although uranium and thorium are similar elements, their behavior is different in

247   reducing and oxidative environments. Thorium is not sensitive to the redox conditions,

248   whereas uranium is precipitated and concentrated only in reducing regimes. Oxidative bottom

249   waters cause U to remain dissolved, hence the sediment would become depleted with respect

250   to U. The PAAS („Post-Archean Australian Shale" standard, thought to represent the upper

251   continental crust) has a U/Th value of 0.26 (McLennan, 1989), whereas that of the C1

252   chondrite is 0.27 (Anders and Grevesse, 1989). Generally, a U/Th ratio > 0.5 is taken to signal

253   anoxic environment (Adams and Weaver, 1958; Fisher and Wignall, 2001; Myers and

254   Wignall, 1987). The U/Th ratio remains low in most of the studied section, except between

255   the samples KBL-K2 and KB-3, where it increases up to 8.5. Significantly, most of the ~2 m

256   thick boundary mudstone, except for its lowermost part, yielded consistently low U/Th

257   values. High values return only in the upper part of the studied section, where the U/Th ratio

258   in several limestone layers (KBL-25, 26, 28) exceeds 2.

259

260   *4.2.3. Cerium anomaly*

261   Several studies demonstrated that the redox sensitivity of Ce is a useful indicator of

262   paleoceanographic conditions (DeBaar et al., 1985, 1988; Elderfield, 1988; German et al.,

263 1995; Hu et al., 1988; Sholkovitz and Schneider, 1991; Schijf and DeBaar, 1995; Dolenec et

264 al., 2001). The abundance of Ce of the carbonate phase in carbonate rocks directly reflects the

265 Ce concentration of the seawater, which in turn is a good indicator of the redox state of the

266 environment. Cerium enters the ocean in its soluble, trivalent state but under oxic bottom

267 water conditions, Ce becomes relatively depleted, as its oxidized form, Ce(IV) is quickly

268 precipitated from the water (Elderfield, 1988; Dolenec et al., 2001), causing a negative Ce

269 anomaly in the REE pattern of the marine carbonates (Dolenec et al., 2001; Hu et al., 1988).

270 However, under anoxic conditions, the behavior of Ce will be similar to other trivalent REE.

271 Thus in the REE pattern of the carbonate phase no pronounced negative Ce anomaly will be

272 visible, resulting a largely flat REE pattern (Dolenec et al., 2001). This can be represented

273 with the Ce/Ce* ratio.

274   In the studied section the Ce/Ce* curve shows an opposite redox signal to the minor

275 redox sensitive elements (Fig. 4). REE measurements could only be performed in the whole-

276 rock samples, not in the separated carbonate fractions. In this case the terrigenous REE

277 content is more dominant in the signal than the carbonate REE, which can be seen in the

278 three-four times higher $\sum$REE of the marls, compared to the carbonates. The Ce-depletion is

279 explained by the dissolution of Ce from the terrigenous component, and staying in the anoxic

280 sea-water, causing an opposite pattern to that seen in the carbonate fraction.

281   The Ce/Ce* is around 0.9 in the marls and 0.75 in the limestone beds. The difference

282 between them is coming from the different terrigenous/carbonate ratio. The carbonate fraction

283 contains a more depleted value, which suggests oxygenated bottom water in the section.

284 Samples from the Kössen Formation yielded more depleted values (0.5) than the Kendlbach

285 Formation limestones, which is explained by the higher carbonate content, and also reflects

286 oxygenated water. The only samples which deviate from this trend are KB-1, 2 and 3. Even

287　though they have lower carbonate content than KBL-K3 and 2, they have more depleted

288　Ce/Ce* values (0.33–0.36).

289　　　To check if the Ce/Ce* value is not an artifact of positive La enrichment, the Pr/Pr*

290　value was calculated (Bau and Dulski, 1996). The values do not show La enrichment.

291

292　**4.3. Rare earth elements (REE)**

293　　　The normalized REE patterns of most samples are remarkably similar to each other

294　and resemble a presumed typical continental source rock (Table 3, Fig. 5). Three features of

295　the REE patterns warrant further discussion: the occasional presence of a Ce-anomaly, HREE

296　enrichment in two samples, and the systematically lower REE content of the limestone

297　samples as compared with the marls. The majority of the observed anomalies are confined to

298　the basal part of the section.

299　　　The two stratigraphically lowermost samples (KBL-K2 and KBL-K3) from the upper

300　part of the Kössen Formation have the lowest amount of REE, but their overall pattern is

301　similar to that of the others. These samples are from the purest limestone with the lowest

302　amount of terrigenous material.

303　　　The next layer is the topmost limestone bed of the Kössen Formation (represented by

304　duplicate samples KBL-0 and KB-1, yielding the same results), which shows a significant

305　HREE enrichment.

306　　　Sample KB-2 was obtained from the 5 cm thick marl layer directly overlying the

307　Kössen Limestone. The abundance of REE in this sample is comparable to most others and

308　some HREE enrichment is also present here but less pronounced than in the underlying layer.

309　　　Sample KB-3 is from a brown, marly layer that contains scattered fish remains (scales

310　and bone fragments). This is reflected in the high apatite content, determined by XRPD as 4

311　wt%, and the high concentration of P_2O_5, determined by whole-rock chemistry as 2.72 wt%

13

312   (Tables 2, 3). The presence of apatite might explain the unusual abundance of REE in this

313   sample, 1.5–3 times higher than in most of the other marl samples, making this sample the

314   richest in REE in the entire studied section. However, there is no HREE enrichment in this

315   sample, contrary to samples KB-1 and KB-2.

316   Starting from sample KB-4, the REE content and REE pattern of the samples are

317   remarkably similar to each other. The only significant difference is that the marly samples

318   contain approximately three times more REE than the limestones. This observation agrees

319   well with the three-to-four times higher amount of detrital terrigenous material in the marls,

320   as calculated from the carbonate content of the samples.

321

322   **4.4. Mineralogy**

323   *4.4.1. Mineral phases from X-ray diffraction*

324   Mineral phases were identified in 22 samples from the section using X-ray powder

325   diffraction (XRPD). Nine samples were further investigated for an in-depth characterization

326   of their clay mineral content, the details of which are beyond the scope of this paper and are

327   presented elsewhere (Zajzon et al., in press). The results are summarized here in Table 3 and

328   Fig. 3.

329   The three main components of the samples are calcite, quartz and clay minerals,

330   beside some less abundant phases such as pyrite, feldspar, apatite, aragonite, gypsum and

331   dolomite. The purest limestone occurs in the Kössen Formation. In the overlying boundary

332   mudstone, the carbonate content drops to 10 wt%. Quartz, clay minerals, feldspars and pyrite

333   appear here as phases not encountered lower in the section. The highest clay mineral content,

334   recorded in sample KB-8, is 45 wt%.

335   The occurrence of pyrite is characteristic for the boundary mudstone, although it is

336   also found at other levels higher in the section. The FeO content of the samples correlates

337 well with the pyrite and goethite phases. The majority of the pyrite is framboidal, as revealed

338 by SEM, indicative of bacterial origin (see below in 4.4.3.). The oxidation of pyrite led to

339 formation of gypsum. The alteration may have occurred either in the outcrop or later, after

340 sample collection. Sample KB-2 contains 4 wt% fluorapatite, which is bound to the unusually

341 abundant fish remains (bones, teeth, scales) in this layer. Sample KB-3 contains 8.4 wt% of

342 aragonite, which likely represents the original shell material of bivalves and foraminifera.

343   The feldspar phases present are albite, sanidine and microcline. The highest amount is

344 registered in the middle to upper part of the boundary mudstone, reaching up to 16 wt%.

345 Sanidine occurs only in the upper part of the boundary mudstone. Dolomite appears in only

346 two samples, accompanied in both by sanidine.

347

348 *4.4.2. Clay mineralogy*

349   In the majority of samples, illite and kaolinite are registered as the main clay minerals

350 with subordinate smectite, and their ratios were monitored to allow environmental and

351 paleoclimatic inferences. Sample KB-1, however, shows a peculiar clay mineral composition

352 very different from the other samples, because it is dominated by low- to medium-charged

353 smectite and also contains vermiculite. These clay minerals commonly represent the alteration

354 products of mafic and/or ultramafic rocks. Upsection, in the boundary mudstone, the clay

355 mineral distribution is characterized by kaolinite $\geq$ illite + muscovite $>>$ smectite. In the

356 higher part of the section a distinctive change in the clay mineral pattern results in illite +

357 muscovite $>>$ kaolinite $>>$ smectite ratios. For more detail, see Zajzon et al. (in press).

358

359 *4.4.3. Scanning electron microscopy (SEM) of pyrite*

360   Six polished samples (KB-1, KBL-K3, 1, 8, 15, 26) were selected for investigation by

361 SEM. All of these samples contain a varying amount of pyrite, which is dominantly

15

362 framboidal. In some of the samples only goethite pseudomorphs were observed, but their

363 shape clearly identifies them as alteration products from pyrite. In many instances the shell of

364 a fossil or part of a microbial mat is recognizable as the locus of pyrite formation. Pyrite also

365 frequently occurs together with apatite. Beside the framboidal form, euhedral pyrite is also

366 common in the samples and both varieties may occur in distinct layers. The framboids are

367 commonly large (0.1–0.2 mm in diameter), and form structures such as mats and spheres,

368 indicative of their formation in the sediment rather than in the water column (Wignall and

369 Newton, 1998; Wilkin et al., 1996). Barite was also found in some layers (e.g. sample KBL-

370 26).

371

372 *4.4.4.* **Micromineralogy of sample KB-1**

373   To follow up on the indication of a possible mafic detrital component suggested by

374 REE data and clay mineralogy, sample KB-1 from the topmost layer of the Kössen Formation

375 was subjected to heavy mineral separation and SEM/EDS examination. The grain size of this

376 micritic limestone is very fine, not more than a few wt% is above 45 μm of the insoluble part.

377 Possible alteration products of volcanic material were indeed detected in this sample, in the

378 form of goethite pseudomorphs after euhedral crystals of pyroxene and amphibole, and pale-

379 green clay spherules that may represent altered glass (Fig. 6).

380   No fresh magmatic minerals were observed, only their alteration products. Goethite

381 pseudomorphs are common, retaining the original shape of abundant pyroxene and

382 subordinate amphibole crystals. These elongated grains are 0.1–0.2 mm in length, and the

383 original crystal shape, the edges and facets are perfectly preserved (Fig. 6d–h). They are

384 easily identifiable as three-dimensional grains in the acid insoluble residue. These

385 pseudomorphs were also observed in the polished samples, where their recognition is more

386   difficult because the shape of their cross-section is less distinctive and often similar to

387   pseudomorphs after pyrite crystals.

388   Pale green, opaque or slightly transparent grains are also present in the sample. Their

389   shapes vary, some of them are perfectly spherical whereas others are subangular (Fig. 6a–c).

390   Their composition, as revealed by EDS, is illite/aluminoceladonite. The shape, size and

391   composition together suggest that these grains represent alteration products of volcanic

392   material, the spheres and rounded particles are most suggestive of altered volcanic glass

393   spherules.

394

395   **5. Discussion**

396   **5.1. Recorders of contemporaneous volcanism**

397   Causal relationship of the ETE and coeval carbon cycle perturbation with CAMP

398   volcanism has been proposed by many authors (e.g. Marzoli et al. 1999, Pálfy 2003, Hesselbo

399   et al. 2007). Support for this hypothesis is primarily provided by dating studies which have

400   established with increasing precision and accuracy the synchrony between CAMP flood

401   basalts (Marzoli et al., 1999, 2004; Nomade et al., 2007) and the Triassic-Jurassic boundary

402   (Pálfy et al., 2000; Schaltegger et al., 2008; Schoene et al., 2010). However, direct

403   stratigraphic evidence for CAMP-derived volcanic material in marine sections has been

404   meager. Where CAMP flows or pyroclastics occur with marine sedimentary rocks e.g. in

405   France and Morocco, precise biostratigraphic dating is hampered by a lack of age-diagnostic

406   fossils (Olsen et al., 2003). Recent studies in terrestrial sections using palynostratigraphy

407   (Cirilli et al., 2009) and conchostracan biostratigraphy (Kozur and Weems, 2010) demonstrate

408   that CAMP volcanism began in the latest Triassic. Available circumstantial evidence for the

409   onset of volcanism include the presence of potentially volcanically derived organic molecules,

410   polycyclic aromatic hydrocarbons, from TJB sediments (van de Schootbrugge et al., 2009)

411   and increase in pCO$_2$ detected both in pedogenic carbonates (Schaller et al., 2011) and by

412   fossil leaf stomatal density (McElwain et al., 1999; Steinthorsdottir et al., 2011).

413   In the Kendlbachgraben section, both the pyroxene and amphibole pseudomorphs and

414   the altered glass spherules found in the topmost Kössen Formation (sample KB-1) are

415   interpreted as volcanic eruption products, most likely representing a distal record of CAMP

416   eruptions. The size and the well preserved rounded original shape of the altered glass

417   spherules suggest airborne origin and transportation. The pyroxene and amphibole crystals

418   fall into the fine ash size range, capable of entering the upper atmosphere within the eruption

419   plume. The well preserved crystal facets and edges rule out the possibility of even short

420   terrestrial transportation that would have caused wear and damage of the grains. The presence

421   of all these "exotic" grains in the pure micritic limestone are best explained as air-fall fine ash

422   particles directly deposited in the marine sedimentary basin.

423   In agreement with the above interpretation, the clay mineral pattern of this layer is also

424   quite different from the other samples. It contains dominantly low- to medium-charged

425   smectite as well as Mg-dominated vermiculite. Typically, these clay minerals occur as

426   alteration products of mafic and ultramafic rocks (Velde and Meunier, 2008; see also Zajzon

427   et al., submitted).

428   A third line of evidence is provided by the REE distribution patterns. The same sample

429   (KB-1) from the topmost layer of Kössen Formation differs from all other samples by a

430   distinctive enrichment of heavy REE. Only the overlying layer (sample KB-2) shows a

431   similar, albeit more subdued HREE enrichment. Such trace element signature, characterized

432   by a V-shaped pattern, may be best interpreted as a mixed signal where the light REEs are

433   derived from the sedimentary component and the enrichement in HREE is sourced from

434   magmatic material. HREE enrichment is characteristic for mantle sources and is known to

435   occur e.g. in N-MORB (Klein, 2003) and ultrabasic rocks (Bodinier and Godard, 2007),

436 where it is carried by mineral phases such as garnets, pyroxenes and amphiboles.

437 Pseudomorphs of the latter two minerals occur in the micromineralogical spectrum of the

438 same sample.

439   The range of REE variation in CAMP extrusives have been reported in several studies

440 and HREE enrichment is clearly documented by Marzoli et al. (2011) in the Preakness and

441 Hook Mt. basalts in the Newark Basin, Sander basalt in the Culpeper basin, and the recurrent

442 basalts in Morocco. The stratigraphic significance of this geochemical similarity to the late

443 rather than early CAMP flows remains to be clarified.

444   To assess the feasibility of CAMP as a source of material preserved at

445 Kendlbachgraben section, it is informative that paleogeographic reconstructions suggest an

446 approximate distance of 2000–2500 km between northeastern CAMP eruptive centers and the

447 marine Eiberg Basin in the western Tethys (Golonka, 2007). Volcanic particulates from

448 eruption plumes are known to travel significant distances in downwind direction (Durant et

449 al., 2010), as recently shown by widespread distribution of ash from the 2010 eruption of

450 Eyjafjallajökull, clearly detected in the Alps, more than 2700 km from Iceland (Flentje et al.,

451 2010). Climate modeling results suggest that the Eiberg basin was downwind of the CAMP at

452 least seasonally during Pangean summers in the Triassic (Wang 2009). Therefore

453 emplacement of CAMP-derived particles in sediments preserved at the Kendlbachgraben

454 section appears plausible. The generally assumed quiet outpouring of flood basalts contradicts

455 the here inferred explosive eruption, capable to produce a high eruption column necessary for

456 long distance particle dispersal. We speculate that at least some of the CAMP volcanism may

457 have been phreatomagmatic, where eruption fissures intersected lakes in the rift basin, thus

458 resulting in unusually explosive eruptions. Because CAMP erupted in multiple pulses, further

459 search for volcanic signatures, perhaps below the topmost Kössen Formation, is warranted to

460 corroborate the evidence presented herein.

461

5.2. Climate-driven changes in detrital input and clay mineralogy

A first-order change in depositional regimes in the Kendlbachgraben section is manifest in the lithostratigraphic boundary between the intraplatform basinal carbonates of the Kössen Formation and clay-rich, fine silicilastics of the boundary mudstone of the Kendlbach Formation. The abrupt change from carbonate-dominated to siliciclastic-dominated sedimentation during the latest Rhaetian may be the stratigraphic expression of several factors. These include (i) a change in weathering regime, i.e. increased influx of terrigenous material and clay under hot and humid conditions, (ii) a biocalcification crisis that triggered a shutdown of the carbonate factory due to CO_2 saturation (Hautmann et al., 2008), (iii) loss of carbonate production due to eutrophication, (iv) rapid sea level rise manifested within a regression-transgression couplet (Hallam and Wignall, 1999), or (v) some combination of these factors.

Our major element and mineral phase distribution data allow quantification of these processes. The major drop in calcite content at the Kössen/Kendlbach formation boundary is clearly shown by XRD data (Table 3) and CaO and total C concentration (Table 1). The boundary mudstone has the highest ratio of clay minerals vs. other detrital components (mainly quartz), as expressed by the Si/Al ratio (Fig. 3) and XRD data (Table 3). Therefore, the initial increase of detrital components was accompanied by peak abundance of clay minerals, marking a significant climatic signal. Sudden climate change to hot and humid conditions leading to intensification of weathering may well explain the terrestrial influx. Co-occurrence of dolomite and feldspar in two samples in the boundary mudstone (KB-6 and 13) suggests further episodic increases in terrestrial input, whereby immature detrital components could reach the depocenter. The amount of the siliciclastic detritus decreases upsection,

485 reflecting either a decrease in humidity and/or transgression and increasing distance from

486 terrigenous source areas.

487   Clay minerals are well-known indicators of climate. In the boundary mudstone the

488 clay mineral composition is kaolinite ≥ illite + muscovite >> smectite > chlorite. The

489 predominance of kaolinite is commonly interpreted to suggest humid climate and intensive

490 terrigenous input. Similar data are known from other TJB sections. Ahlberg et al. (2003)

491 report a kaolinite ≈ illite >> chlorite and smectite (I/S) clay pattern from Rhaetian-Hettangian

492 terrestrial sedimentary successions, and kaolinite ≈ illite > variable smectite >> chlorite

493 pattern from shallow marine deposits (Höganäs Formation) in southern Sweden. These

494 authors concluded that the original detrital composition was better preserved in the shallow

495 marine settings and infer warm, humid conditions and intense weathering. High amounts of

496 kaolinite are also reported from the topmost Triassic *Triletes* beds in Germany, interpreted to

497 reflect strongly leached soils that become enriched in aluminium (van de Schootbrugge et al.,

498 2009). A pronounced increase in kaolinite also characterizes the TJB in sections of the Tatra

499 Mts. (Slovakia), where a climatic driver was similarly invoked (Michalík et al., 2010).

500   Higher up in the Kendlbachgraben section, above the boundary mudstone, the clay

501 mineral pattern changes to illite + muscovite >> kaolinite >> smectite, which corresponds to a

502 less humid and less hot climate. Therefore our results suggest that the extreme greenhouse

503 conditions around the TJB were initially forced by volcanic CO_2 degassing but had a limited

504 temporal extent, which nevertheless coincided with the ETE and the onset of both the initial

505 and main negative carbon anomalies.

506

507 **5.3. Changes in redox conditions**

508   Marine anoxia often accompanies greenhouse climate maxima due to reduced ocean

509 circulation, and plays a role in extinction events. Specifically, oxygen-depleted facies across

510   the TJB were noted from northwest Europe (Hallam, 1995). Although no longer a favoured

511   scenario, this possible cause is still often considered for the end-Triassic extinction (Hallam

512   and Wignall, 1997). However, in sections in Britain, anoxic sediments were shown to occur

513   only above the main end-Triassic extinction horizon and initial carbon isotope excursion

514   (Wignall and Bond, 2008). Within our dataset, the occurrence of pyrite, distribution of redox-

515   sensitive elements, and relative abundance of Ce among the other REE permit evaluation if

516   dysoxic or anoxic conditions developed around the TJB in the Kendlbachgraben section.

517   Peak values of Fe and S within the boundary mudstone (see 4.1.) are tied to the

518   occurrence of pyrite, as evidenced by XRD data (Table 3). SEM analyses reveal that

519   framboidal pyrite of large size (up to 0.1–0.2 mm in diameter) is predominant, that suggests

520   formation within the sediment under reducing conditions (Wignall et al., 2005), but it does

521   not require the presence of anoxic bottom water.

522   Water column oxygenation is suggested by the redox-sensitive elements, whose

523   concentration remains low throughout the section (Fig. 4). Enrichment of these elements is

524   most pronounced in the lowermost 10 cm of the boundary mudstone (samples KB-1, 2 and 3),

525   which are therefore permissive of reducing environment above the sediment/water interface.

526   However, this observation contradicts the presence of benthic bivalves, but is compatible with

527   the abundance of fish remains and phosphate in KB-3. A second interval with a somewhat

528   elevated concentration of redox-sensitive elements is encountered near the top of the studied

529   section, in the early Hettangian.

530   As an independent redox indicator, the U/Th ratio remains low in most of the studied

531   section, except between the samples KBL-K2 and KB-3, where it goes up to as high as 8.5,

532   possibly indicating oxygen-depleted conditions during deposition of the topmost Kössen

533   Formation and the lowermost part of the boundary mudstone. This signal is comparable to

534   that obtained by McRoberts et al. (1997) from another section in western Austria.

535   Alternatively, the U/Th ratio at this level may also be influenced by volcanic input.

536   Interpretation of changes in Ce abundance in the section is not straightforward. As

537   analyses were carried out on bulk samples, the Ce signal of marine carbonate is mixed with

538   that of the detrital component. Higher carbonate content is correlated with negative shifts in

539   Ce concentration, suggesting that the marine carbonate is depleted in Ce, which in turn points

540   to oxidative water favoring precipitation of trivalent Ce. Anoxic bottom waters are not

541   indicated by the Ce signal.

542   In summary, widespread anoxia near the TJB is not compatible with our data; oxygen-

543   depleted bottom water may only characterized brief intervals during the earliest phase of

544   boundary mudstone deposition, coinciding with the temperature maximum inferred from the

545   clay mineral climate proxy. Several other sections in the Eiberg Basin contain the red

546   Schattwald beds immediately below the TJB; this hematite-bearing unit is a regional

547   stratigraphic indicator of oxidized facies (Krystyn et al. 2005).

548

549 **6. Conclusions**

550   Our study has focused on a Triassic-Jurassic boundary (TJB) section at

551   Kendlbachgraben in the Northern Calcareous Alps, within the same intraplatform basin as the

552   recently selected base Jurassic Global Stratotype Section and Point. The much debated

553   causation of the end-Triassic mass extinction (ETE) and broadly synchronous major carbon

554   isotope excursions instigated our research. In particular, the aim of our multi-approach study

555   was to search for stratigraphic evidence in this marine section for distant volcanism of the

556   Central Atlantic Magmatic Province (CAMP), widely regarded as a trigger of interrelated

557   global climatic, environmental and biotic changes. The key findings of our study are the

558   following:

559   1) The topmost bed of the otherwise pure micritic limestone of the Rhaetian Kössen

560   Formation contains goethite pseudomorphs of euhedral pyroxene and amphibole crystals.

561   Such grains in this depositional environment are thought to represent distal fallout of a

562   volcanic ash cloud.

563   2) The same bed also yielded rounded or spherical grains of illite/aluminoceladonite

564   composition, interpreted as alteration products of airborne volcanic glass particles. Additional

565   clay minerals restricted to this bed are low- to medium-charged smectite and Mg-vermiculite,

566   commonly formed by alteration of mafic volcanic material.

567   3) Another characteristic feature of this bed is its enrichment in heavy rare earth elements, a

568   pattern noted from some mantle-derived mafic volcanics and documented from several flow

569   units of the CAMP. This set of observed features is best explained by mafic volcanic material

570   admixed to the carbonate from distal ash fallout, likely related to a CAMP eruption.

571   4) After the deposition of this layer, carbonate sedimentation of the Kössen Formation

572   abruptly gave way to clay-rich, terrigenous sedimentation of the boundary mudstone and the

573   overlying alternating mudstone, marl and marly limestone beds (topmost Rhaetian to lower

574   Hettangian Tiefengraben Member of the Kendlbach Formation). Previous authors also noted

575   the disappearance of Triassic ammonoid and conodont faunas and the onset of the initial

576   carbon isotope excursion at this level. Thus this local facies change is best regarded as the

577   record of far-reaching global changes immediately preceding the TJB, at the time of the ETE.

578   5) Elemental geochemistry and clay mineralogy helped quantify the increase in terrigenous

579   and clay mineral input at the expense of carbonate production. The lowermost 2 m of the

580   boundary mudstone is particularly rich in kaolinite, signifying a sudden change in weathering

581   regime possibly related to transient extreme greenhouse climate in the hinterland.

582   6) Abundant framboidal pyrite is present in the TJB interval, but its size suggests formation

583   within the sediment rather than in an anoxic water column. Redox-sensitive minor elements

584   and Ce also fail to support widespread oxygen-depleted conditions in the marine basin. Thus

585   anoxia does not appear to play a fundamental role in the extinction.

586   In summary, independent geochemical, micromineralogical and clay mineralogical lines of

587   evidence provide as yet the best direct link between end-Triassic volcanism and the marine

588   stratigraphic record, where extinction and the carbon isotope anomaly are also present. The

589   new data provide further support for a scenario where CAMP volcanism induced climate and

590   other environmental change which in turn triggered the ETE and is also reflected in the TJB

591   carbon isotope anomalies.

592

602

603   **References**

604   Adams, J.A.S., Weaver, C.E., 1958. Thorium-to-uranium ratios as indicators of sedimentary

605   processes: example of concept of geochemical facies. Am. Assoc. Petrol. Geol.

606   Bulletin 42: 387–430.

607   Ahlberg A., Olsson I., Šimkevičius P., 2003. Triassic–Jurassic weathering and clay mineral

608   dispersal in basement areas and sedimentary basins of southern Sweden. Sediment.

609   Geol. 161: 15–29.

610   Alroy, J., 2008. Dynamics of origination and extinction in the marine fossil record. Proc. Natl.

611   Acad. Sci. U. S. A. 105: 11536–11542.

612   Anders, E., Grevesse, N., 1989. Abundances of the elements: Meteoritic and solar. Geochim.

613   Cosmochim. Acta 53: 197–214.

614   Bau, M ., Dulski, P., 1996. Distribution of yttrium and rare-earth elements in the Penge and

615   Kuruman iron-formations, Transvaal Supergroup, South Africa. Precambrian Res. 79:

616   37–55.

617   Berner, R.A., 1971. The synthesis of framboidal pyrite. Econ. Geol. 64: 383–384.

618   Bodinier, J.L., Godard, M., 2007. Orogenic, Ophiolitic, and Abyssal Peridotites. In: Heinrich,

619   D.H., Karl, K.T. (Eds.), Treatise on Geochemistry. Pergamon, Oxford, pp. 1–73.

620   Bonis, N.R., Kürschner, W.M., Krystyn, L., 2009. A detailed palynological study of the

621   Triassic-Jurassic transition in key sections of the Eiberg Basin (Northern Calcareous

622   Alps, Austria). Rev. Palaeobot. Palynol. 156: 376–400.

623   Calvert, S. E., 1976. The mineralogy and geochemistry of nearshore sediments. In: Riley, J.P.,

624   Chester, R. (Eds.), Chemical Oceanography (vol. 6). Academic Press, New York, pp.

625   187–280.

626   Carter, E.S., Hori, R.S., 2005. Global correlation of the radiolarian faunal change across the

627   Triassic-Jurassic boundary. Can. J. Earth Sci. 42: 777–790.

628   Cirilli, S., Marzoli, A., Tanner, L., Bertrand, H., Buratti, N., Jourdan, F., Bellieni, G., Kontak,

629   D., Renne, P.R., 2009. Latest Triassic onset of the Central Atlantic Magmatic

630   Province (CAMP) volcanism in the Fundy Basin (Nova Scotia): New stratigraphic

631   constraints. Earth Planet. Sci. Lett. 286: 514–525.

632   DeBaar, H.J.W., Bacon, M.P., Brewer, P.G., Bruland, K.W., 1985. Rare earth elements in the

633   Pacific and Atlantic oceans. Geochim. Cosmochim. Acta 49: 1943–1960.

634   DeBaar, H.J.W., German, C.R., Elderfield, H., Gaans, P.V., 1988. Rare earth element

635   distributions in anoxic waters of the Carriaco Trench. Geochim. Cosmochim. Acta 52:

636   1203–1219.

637   Dolenec, T., Lojen, S., Ramovs, A., 2001. The Permian–Triassic boundary in Western

638   Slovenia (Idrijca Valley section): magnetostratigraphy, stable isotopes, and elemental

639   variations. Chem. Geol. 175: 175–190.

640   Durant, A.J., Bonadonna, C., Horwell, C.J., 2010. Atmospheric and environmental impacts of

641   volcanic particulates. Elements 6: 235–240.

642   Elderfield, H., 1988. The oceanic chemistry of the rare-earth elements. Philos. Trans. R. Soc.

643   London, Ser. A 325: 105–126.

644   Fisher, Q.J., Wignall, P.B. (2001): Palaeoenvironmental controls on the uranium distribution

645   in an Upper Carboniferous black shale (*Gastrioceras listeri* Marine Band) and

646   associated strata; England. Chem. Geol. 175: 605–621.

647   Flentje, H., Claude, H., Elste, T., Gilge, S., Köhler, U., Plass-Dülmer, C., Steinbrecht, W.,

648   Thomas, W., Werner, A., Fricke, W., 2010. The Eyjafjallajökull eruption in April

649   2010 – detection of volcanic plume using in-situ measurements, ozone sondes and

650   lidar-ceilometer profiles. Atmosph. Chem. Phys. 10: 10085–10092.

651   Flügel, E., 2002. Triassic reef patterns. In: Kiessling, W., Flügel, E., Golonka, J. (Eds.),

652   Phanerozoic Reef Patterns. SEPM (Soc. Sed. Geol.) Spec. Pub. 72: 391–464.

653   Galli, M.T., Jadoul, F., Bernasconi, S.M., Cirilli, S., Weissert, H., 2007. Stratigraphy and

654   palaeoenvironmental analysis of the Triassic-Jurassic transition in the western

655   Southern Alps (Northern Italy). Palaeogeogr. Palaeoclimat. Palaeoecol. 244: 52–70.

656 German, C.R., Masuzawa, T., Greaves, M.J., Elderfield, H., Edmond, J.M., 1995. Dissolved
657   rare earth elements in the Southern Ocean: cerium oxidation and the influence of
658   hydrography. Geochim. Cosmochim. Acta 59: 1551–1558.

659 Golebiowski, R., 1990. Facial and faunistic changes from Triassic to Jurassic in the Northern
660   Calcareous Alps (Austria). Cah. Univ. Cathol. Lyon, Sér. Sci. 3: 175–184.

661 Golebiowski, R., Braunstein, R.E., 1988. A Triassic/Jurassic boundary section in the northern
662   Calcareous Alps (Austria). Ber. Geol. Bundesanst. 15: 39–46.

663 Golonka, J., 2007. Late Triassic and Early Jurassic palaeogeography of the world.
664   Palaeogeogr. Palaeoclimat. Palaeoecol. 244: 297–307.

665 Guex, J., Bartolini, A., Atudorei, V., Taylor, D., 2004. High-resolution ammonite and carbon
666   isotope stratigraphy across the Triassic-Jurassic boundary at New York Canyon
667   (Nevada). Earth Planet. Sci. Lett. 225: 29–41.

668 Hallam, A., 1990. Correlation of the Triassic-Jurassic boundary in England and Austria. J.
669   Geol. Soc., Lond. 147: 421–424.

670 Hallam, A., 1995. Oxygen-restricted facies of the basal Jurassic of northwest Europe. Hist.
671   Biol. 10: 247–257.

672 Hallam, A., Goodfellow, W.D., 1990. Facies and geochemical evidence bearing on the end-
673   Triassic disappearance of the Alpine reef ecosystem. Historical Biology 4: 131-138.

674 Hallam, A., Wignall, P.B., 1997. Mass Extinctions and Their Aftermath. Oxford University
675   Press, Oxford.

676 Hallam, A., Wignall, P.B., 1999. Mass extinctions and sea-level changes. Earth-Sci. Rev. 48:
677   217–250.

678 Hautmann, M., 2004. Effect of end-Triassic CO_2 maximum on carbonate sedimentation and
679   marine mass extinction. Facies 50: 257–261.

680   Hautmann, M., Benton, M.J., Tomasovych, A., 2008. Catastrophic ocean acidification at the

681   Triassic-Jurassic boundary. N. Jb. Geol. Paläont. Abh. 249: 119–127.

682   Hesselbo, S.P., Robinson, S.A., Surlyk, F., Piasecki, S., 2002. Terrestrial and marine mass

683   extinction at the Triassic–Jurassic boundary synchronized with major carbon-cycle

684   perturbation: A link to initiation of massive volcanism? Geology 30: 251–254.

685   Hesselbo, S.P., McRoberts, C.A., Pálfy, J., 2007. Triassic–Jurassic boundary events:

686   Problems, progress, possibilities. Palaeogeogr. Palaeoclimat. Palaeoecol. 244: 1–10.

687   Hillebrandt, A. von, Krystyn, L., 2009. On the oldest Jurassic ammonites of Europe (Northern

688   Calcareous Alps, Austria) and their global significance. N. Jb. Geol. Paläont. Abh.

689   253: 163–195.

690   Hillebrandt, A. von, Krystyn, L., Kuerschner, W.M., 2007. A candidate GSSP for the base of

691   the Jurassic in the Northern Calcareous Alps (Kuhjoch section, Karwendel Mountains,

692   Tyrol, Austria). Int. Subcomm. Jurass. Stratigr. Newsl. 34: 2–20.

693   Hu, X., Wang, Y.L., Schmitt, R.A., 1988. Geochemistry of sediments on the Rio Grande Rise

694   and the redox evolution of the south Atlantic Ocean. Geochim. Cosmochim. Acta 52:

695   201–207.

696   Kiessling, W., Aberhan, M., Brenneis, B., Wagner, P.J., 2007. Extinction trajectories of

697   benthic organisms across the Triassic-Jurassic boundary. Palaeogeogr. Palaeoclimat.

698   Palaeoecol. 244: 201–222.

699   Klein, E.M., 2003. Geochemistry of the igneous oceanic crust. In: Heinrich, D.H., Karl, K.T.

700   (Eds.), Treatise on Geochemistry. Pergamon, Oxford, pp. 433–463.

701   Kozur, H.W., Weems, R.E., 2010. The biostratigraphic importance of conchostracans in the

702   continental Triassic of the northern hemisphere. In: Lucas, S.G. (Ed.), The Triassic

703   Timescale. Geol. Soc. Lond., Spec. Publ. 334: 315–417.

704 Krystyn, L., Böhm, F., Kürschner, W., Delecat, S., 2005. The Triassic–Jurassic boundary in
705   the Northern Calcareous Alps. In: Pálfy, J., Ozsvárt, P. (Eds.), Program, Abstracts and
706   Field Guide, 5th Field Workshop of IGCP 458 Project (Tata and Hallein), pp. A1–A14.

707 Kürschner, W.M., Bonis, N.R., Krystyn, L., 2007. Carbon-isotope stratigraphy and
708   palynostratigraphy of the Triassic-Jurassic transition in the Tiefengraben section —
709   Northern Calcareous Alps (Austria). Palaeogeogr. Palaeoclimat. Palaeoecol. 244: 257–
710   280.

711 Linzer, H.-G., Ratschbacher, L., Frisch, W., 1995. Transpressional collision structures in the
712   upper crust: the fold-thrust belt of the Northern Calcareous Alps. Tectonophysics 242:
713   41–61.

714 Marzoli, A., Renne, P.R., Piccirillo, E.M., Ernesto, M., Bellieni, G., De Min, A., 1999.
715   Extensive 200-million-year-old continental flood basalts of the Central Atlantic
716   Magmatic Province. Science 284: 616–618.

717 Marzoli, A., Bertrand, H., Knight, K.B., Cirilli, S., Buratti, N., Verati, C., Nomade, S., Renne,
718   P.R., Youbi, N., Martini, R., Allenbach, K., Neuwerth, R., Rapaille, C., Zaninetti, L.,
719   Bellieni, G., 2004. Synchrony of the Central Atlantic magmatic province and the
720   Triassic-Jurassic boundary climatic and biotic crisis. Geology 32: 973–976.

721 Marzoli, A., Jourdan, F., Puffer, J.H., Cuppone, T., Tanner, L.H., Weems, R.E., Bertrand, H.,
722   Cirilli, S., Bellieni, G., De Min, A., 2011. Timing and duration of the Central Atlantic
723   magmatic province in the Newark and Culpeper basins, eastern U.S.A. Lithos 122:
724   175–188.

725 McElwain, J.C., Punyasena, S.W., 2007. Mass extinction events and the plant fossil record.
726   Trends Ecol. Evol. 22: 548–557.

727 McElwain, J.C., Beerling, D.J., Woodward, F.I., 1999. Fossil plants and global warming at
728   the Triassic-Jurassic Boundary. Science 285: 1386–1390.

729 McElwain, J.C., Popa, M.E., Hesselbo, S.P., Haworth, M., Surlyk, F., 2007. Macroecological

730   responses of terrestrial vegetation to climatic and atmospheric change across the

731   Triassic/Jurassic boundary in East Greenland. Paleobiology 33: 547–573.

732 McGhee, G.R., Sheehan, P.M., Bottjer, D.J., Droser, M.L., 2004. Ecological ranking of

733   Phanerozoic biodiversity crises: ecological and taxonomic severities are decoupled.

734   Palaeogeogr. Palaeoclimat. Palaeoecol. 211: 289–297.

735 McLennan, S.M., 1989. Rare earth elements in sedimentary rocks: influence of provenance

736   and sedimentary processes. In: Lipin, B.R., McKay, G.A. (Eds.), Geochemistry and

737   mineralogy of rare earth elements. Rev. Mineral. 21: 169–200.

738 McRoberts, C.A., Furrer, H., Jones, D.S., 1997. Palaeoenvironmental interpretation of a

739   Triassic-Jurassic boundary section from Western Austria based on palaeoecological

740   and geochemical data. Palaeogeogr. Palaeoclimat. Palaeoecol. 136: 79–95.

741 Michalík, J., Biroň, A., Lintnerová, O., Götz, A.E., Ruckwied, K., 2010. Climate change at

742   the Triassic/Jurassic boundary in the northwestern Tethyan realm, inferred from

743   sections in the Tatra Mountains (Slovakia). Acta Geol. Pol. 60: 535–548.

744 Morante, R., Hallam, A., 1996. Organic carbon isotopic record across the Triassic-Jurassic

745   boundary in Austria and its bearing on the cause of the mass extinction. Geology 24:

746   391–394.

747 Morbey, S.J., 1975. The palynostratigraphy of the Rhaetian stage, Upper Triassic, in the

748   Kendelbachgraben, Austria. Palaeontographica, Abt. B 152: 1–75.

749 Myers, K.J., Wignall, P.B., 1987. Understanding Jurassic organic-rich mudrocks–new

750   concepts using gamma-ray spectrometry and palaeoecology: examples from the

751   Kimmeridge Clay of Dorset and the Jet rock of Yorkshire. In: Leggett, J.K., Zuffa,

752   G.G. (Eds.), Marine Clastic Sedimentology. Graham and Trotman, London, pp. 172–

753   189.

754   Nomade, S., Knight, K.B., Beutel, E., Renne, P.R., Verati, C., Feraud, G., Marzoli, A., Youbi,

755   N., Bertrand, H., 2007. Chronology of the Central Atlantic Magmatic Province:

756   Implications for the Central Atlantic rifting processes and the Triassic-Jurassic biotic

757   crisis. Palaeogeogr. Palaeoclimat. Palaeoecol. 244: 326–344.

758   Olsen, P.E., Shubin, N.H., Anders, M.H., 1987. New Early Jurassic tetrapod assemblages

759   constrain Triassic-Jurassic tetrapod extinction event. Science 237: 1025–1029.

760   Olsen, P.E., Kent, D.V., Sues, H.-D., Koeberl, C., Huber, H., Montanari, A., Rainforth, E.C.,

761   Fowell, S.J., Szajna, M.J., Hartline, B.W., 2002. Ascent of dinosaurs linked to an

762   iridium anomaly at the Triassic-Jurassic boundary. Science 296: 1305–1307.

763   Olsen, P.E., Kent, D.V., Et-Touhami, M., Puffer , J., 2003. Cyclo-, magneto-, and bio-

764   stratigraphic constraints on the duration of the CAMP event and its relationship to the

765   Triassic-Jurassic boundary. In: Hames, W.E., McHone, J.G., Renne, P.R., Ruppel, C.

766   (Eds), The Central Atlantic Magmatic Province: Insights from fragments of Pangea.

767   Geophysical Monograph Series 136: 7–32.

768   Pálfy, J., 2003. Volcanism of the Central Atlantic Magmatic Province as a potential driving

769   force in the end-Triassic mass extinction. In: Hames, W.E., McHone, J.G., Renne,

770   P.R., Ruppel, C. (Eds), The Central Atlantic Magmatic Province: Insights from

771   fragments of Pangea. AGU Geophysical Monograph Series 136: 255–267.

772   Pálfy, J., Mortensen, J.K., Carter, E.S., Smith, P.L., Friedman, R.M., Tipper, H.W., 2000.

773   Timing the end-Triassic mass extinction: First on land, then in the sea? Geology 28:

774   39–42.

775   Pálfy, J., Demény, A., Haas, J., Hetényi, M., Orchard, M., Vető, I., 2001. Carbon isotope

776   anomaly and other geochemical changes at the Triassic-Jurassic boundary from a

777   marine section in Hungary. Geology 29: 1047–1050.

778   Raup, D.M., Sepkoski, J.J., Jr., 1982. Mass extinctions in the marine fossil record. Science

779   215: 1501–1503.

780   Ruhl, M., Kuerschner, W.M., Krystyn, L., 2009. Triassic-Jurassic organic carbon isotope

781   stratigraphy of key sections in the western Tethys realm (Austria). Earth Planet. Sci.

782   Lett. 281: 169–187.

783   Schaller, M.F., Wright, J.D., Kent, D.V., 2011. Atmospheric pCO$_2$ perturbations associated

784   with the Central Atlantic Magmatic Province. Science 331: 1404–1409.

785   Schaltegger, U., Guex, J., Bartolini, A., Schoene, B., Ovtcharova, M., 2008. Precise U-Pb age

786   constraints for end-Triassic mass extinction, its correlation to volcanism and

787   Hettangian post-extinction recovery. Earth Planet. Sci. Lett. 267: 266–275.

788   Schijf, J., DeBaar, H.J.W., 1995. Rare earth element exchange through the Bosporus: the

789   Black Sea as a net source of REEs to the Mediterranean Sea. Geochim. Cosmochim.

790   Acta 59: 3503–3509.

791   Schoene, B., Guex, J., Bartolini, A., Schaltegger, U., Blackburn, T.J., 2010. Correlating the

792   end-Triassic mass extinction and flood basalt volcanism at the 100 ka level. Geology

793   38: 387–390.

794   Sepkoski, J.J., 1981. A factor analytic description of the Phanerozoic marine fossil record.

795   Paleobiology 7: 36–53.

796   Sepkoski, J.J., 1993. Ten years in the library: new data confirm paleontological patterns.

797   Paleobiology 19: 43–51.

798   Sholkovitz, E.R., Schneider, D.L., 1991. Cerium redox cycles and rare earth elements in the

799   Sargasso Sea. Geochim. Cosmochim. Acta 55: 2737–2743.

800   Steinthorsdottir, M., Jeram, A.J., McElwain, J.C., 2011. Extremely elevated CO$_2$

801   concentrations at the Triassic/Jurassic boundary. Palaeogeogr. Palaeoclimat.

802   Palaeoecol. 308: 418–432.

803   Suess, E., Mojsisovics, E., 1868. Studien über die Trias- und Jurabildungen in den östlichen

804   Alpen. Die Gebirgsgruppe des Osterhornes. Jb. kais.-kön. geol. Reichanst. 18: 168–

805   200.

806   van de Schootbrugge, B., Quan, T.M., Lindstrom, S., Puttmann, W., Heunisch, C., Pross, J.,

807   Fiebig, J., Petschick, R., Rohling, H.G., Richoz, S., Rosenthal, Y., Falkowski, P.G.,

808   2009. Floral changes across the Triassic/Jurassic boundary linked to flood basalt

809   volcanism. Nature Geosci. 2: 589–594.

810   Velde, B., Meunier, A., 2008. The origin of clay minerals in soils and weathered rocks.

811   Springer, Berlin, Heidelberg. Vine, J. D., Tourtelot, E. B., 1970. Geochemistry of

812   black shale deposits – a summary report. Econ. Geol. 65: 253–272.

813   Wang, P., 2009. Global monsoon in a geological perspective. Chin. Sci. Bull. 54: 1113–1136.

814   Ward, P.D., Haggart, J.W., Carter, E.S., Wilbur, D., Tipper, H.W., Evans, T., 2001. Sudden

815   productivity collapse associated with the Triassic-Jurassic boundary mass extinction.

816   Science 292: 1148–1151.

817   Whiteside, J.H., Olsen, P.E., Kent, D.V., Fowell, S.J., Et-Touhami, M., 2007. Synchrony

818   between the Central Atlantic magmatic province and the Triassic-Jurassic mass-

819   extinction event? Palaeogeogr. Palaeoclimat. Palaeoecol. 244: 345–367.

820   Wignall, P. B., Newton, R., 1998. Pyrite framboid diameter as a measure of oxygen

821   deficiency in ancient mudrocks. Am. J. Sci. 298: 537–552.

822   Wignall, P.B., Newton, R., Brookfield, M.E., 2005. Pyrite framboid evidence for oxygen-poor

823   deposition during the Permian-Triassic crisis in Kashmir. Palaeogeogr. Palaeoclimat.

824   Palaeoecol. 216: 183–188.

825   Wilkin, R.T., Barnes, H.L., Brantley, S.L., 1996. The size distribution of framboidal pyrite in

826   modern sediments: An indicator of redox conditions. Geochim. Cosmochim. Acta 60:

827   3897–3912.

828   Zajzon, N., Kristály, F., Pálfy, J., Németh, T., in press. Detailed clay mineralogy of the

829   Triassic-Jurassic boundary section at Kendlbachgraben (Northern Calcareous Alps,

830   Austria). Clay Minerals – Journal of Fine Particle Science.

831

832

Figure captions

834

835   Fig. 1. Location of Triassic-Jurassic boundary sections at Kendlbachgraben (subject of this

836   study) and Kuhjoch (Global Stratotype Section and Point, GSSP) within the Eiberg

837   basin, shown on a schematic tectonic map of the Northern Calcareous Alps (modified

838   from Hillebrandt and Krystyn, 2009).

839   Fig. 2. Stratigraphic correlation of the Kendlbachgraben section with the basal Jurassic GSSP

840   at Kuhjoch and the Tiefengraben sections (based on data in Hillebrandt et al., 2007;

841   Kürschner et al., 2007; Ruhl et al., 2009). The simplified lithologic logs are drawn to

842   the same scale; white denotes limestone and calcareous marl, dark grey denotes

843   claystone and clayey marl, including the boundary mudstone. Reddish claystone of the

844   Schattwals beds are marked by light grey. GSSP marks the officially agreed upon

845   level of the Triassic-Jurassic boundary in the stratotype section. ICIE: Initial carbon

846   isotope excursion. MCIE: Beginning of the main carbon isotope excursion. Lines with

847   arrowhead mark the first and last occurrence datum of diagnostic taxa. *C. m.*:

848   *Choristoceras marshi*; *C. t.*: *Cerebropollenites thiergartii*; *P. s.*: *Psiloceras spelae*; *P.*

849   *t.*: *Psiloceras tilmanni*.

850   Fig. 3. Stratigraphy, mineral composition, and Si and Al elemental geochemistry of the

851   Kendlbachgraben section. Sampled horizons are marked and labeled along the

852   lithologic column. Horizontal bars show carbonate content and other mineral phases

853   from XRD. Colors (and abbreviations) for mineral phases of the samples: blue (cal)–

854   calcite, gray (Q)–quartz, brown (cl)–clay minerals, green (F)–feldspar, black (P)–

855   pyrite, orange (a)–apatite, red (Ar)–aragonite, pink (D)–dolomite. The curve in the

856   same panel shows changes in the carbonate content measured by XRD or from the

857   chemical analyses (circles). Main changes in clay mineralogy are indicated. Panel to

858   the right shows the Si/Al ratio (on logarithmic scale). Solid markers denote marl

859   samples, open markers denote limestone samples. ICIE: Initial carbon isotope

860   excursion. MCIE: Beginning of the main carbon isotope excursion. Line with

861   arrowhead marks the last occurrence datum of *Choristoceras marshi* (*C. m.*).

862   Fig. 4. Stratigraphy, and minor and trace elemental geochemistry of the Kendlbachgraben

863   section. Sampled horizons are marked and labeled along the lithologic column. Panels

864   to the right show Th-normalized values of redox-sensitive elements (note the

865   combined scale: bld–below detection limit, logarithmic (0.001–1), normal (1–25),

866   value shown >25), Ce content (in ppm, upper scale, black line), and Ce/Ce* (lower

867   scale, purple line). Solid markers denote marl samples, open markers denote limestone

868   samples. ICIE: Initial carbon isotope excursion. MCIE: Beginning of the main carbon

869   isotope excursion. Line with arrowhead marks the last occurrence datum of

870   *Choristoceras marshi* (*C. m.*).

871   Fig. 5. Chondrite-normalized REE distribution patterns (spider diagrams) from the

872   Kendlbachgraben section. Colored lines and larger markers denote samples explained

873   in the text and named in the legend, grey lines refer to all other limestone samples,

874   black lines refer to all other marl samples.

875   Fig. 6. SEM photomicrographs of assumed volcanically-derived mineral grains from sample

876   KB-1 (latest Triassic, from top of Kössen Formation). a-c – illite-aluminoceladonite

877   spherules, presumed altered volcanic glass droplets; d-f – goethite pseudomorphs after

878   pyroxene crystals; g-h – goethite pseudomorphs after amphibole crystals.

879

880

881   **Tables**

882

883   Table 1. Data of major and trace element chemical analyses

884   Table 2. Data of REE chemical analyses

885   Table 3. Percent abundance of mineral phases from XRD analyses

886

- New data from a classical Triassic-Jurassic boundary section, correlated with the GSSP

- First direct evidence for CAMP-derived material in a well-dated marine section

- Amphibole and pyroxene pseudomorphs and altered glass spherules from distal ash fall

- HREE enrichment and clay minerals also point to mantle-derived volcanic component

- Abundant kaolinite records change in weathering under extreme greenhouse climate

Figure 3
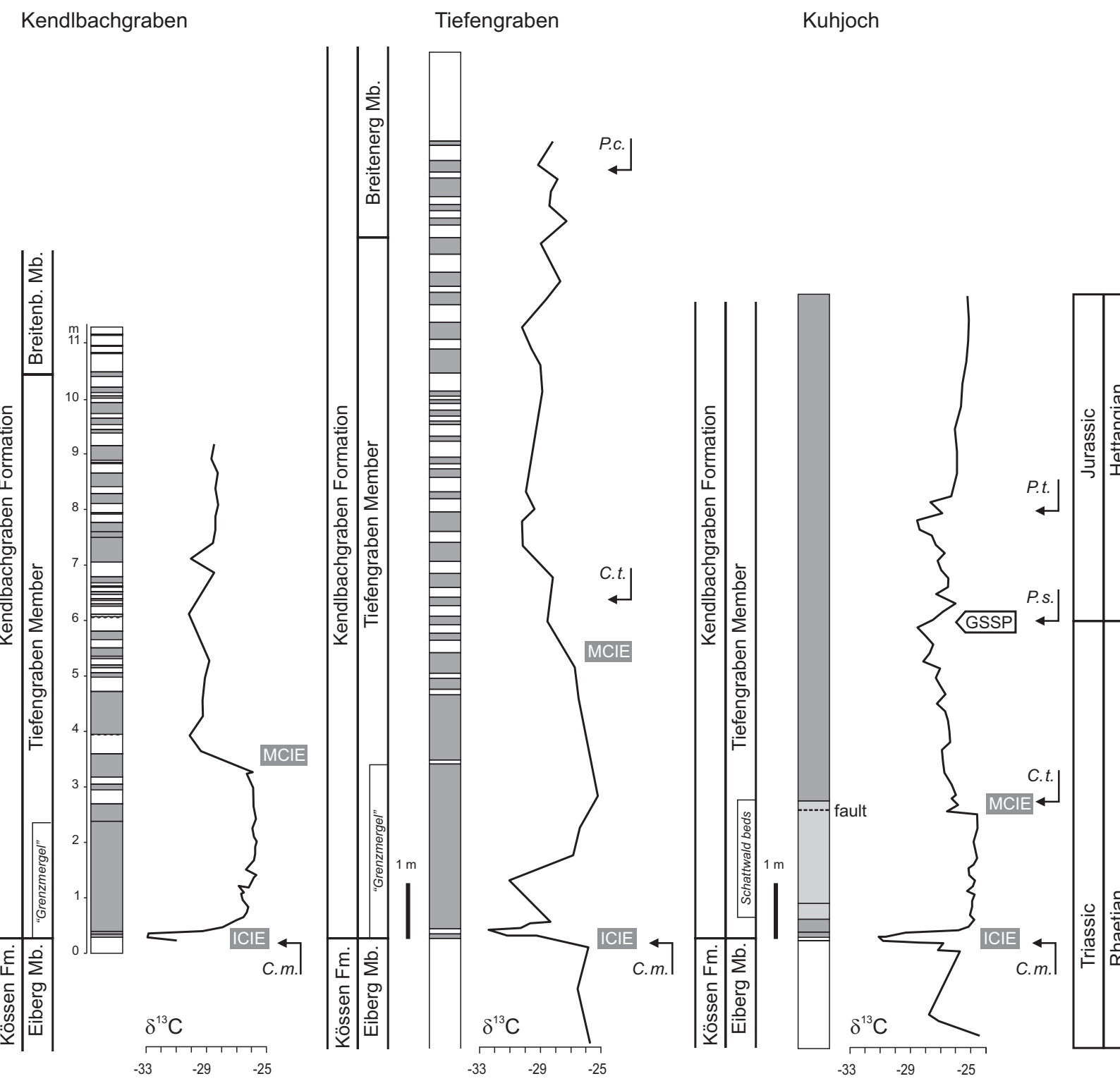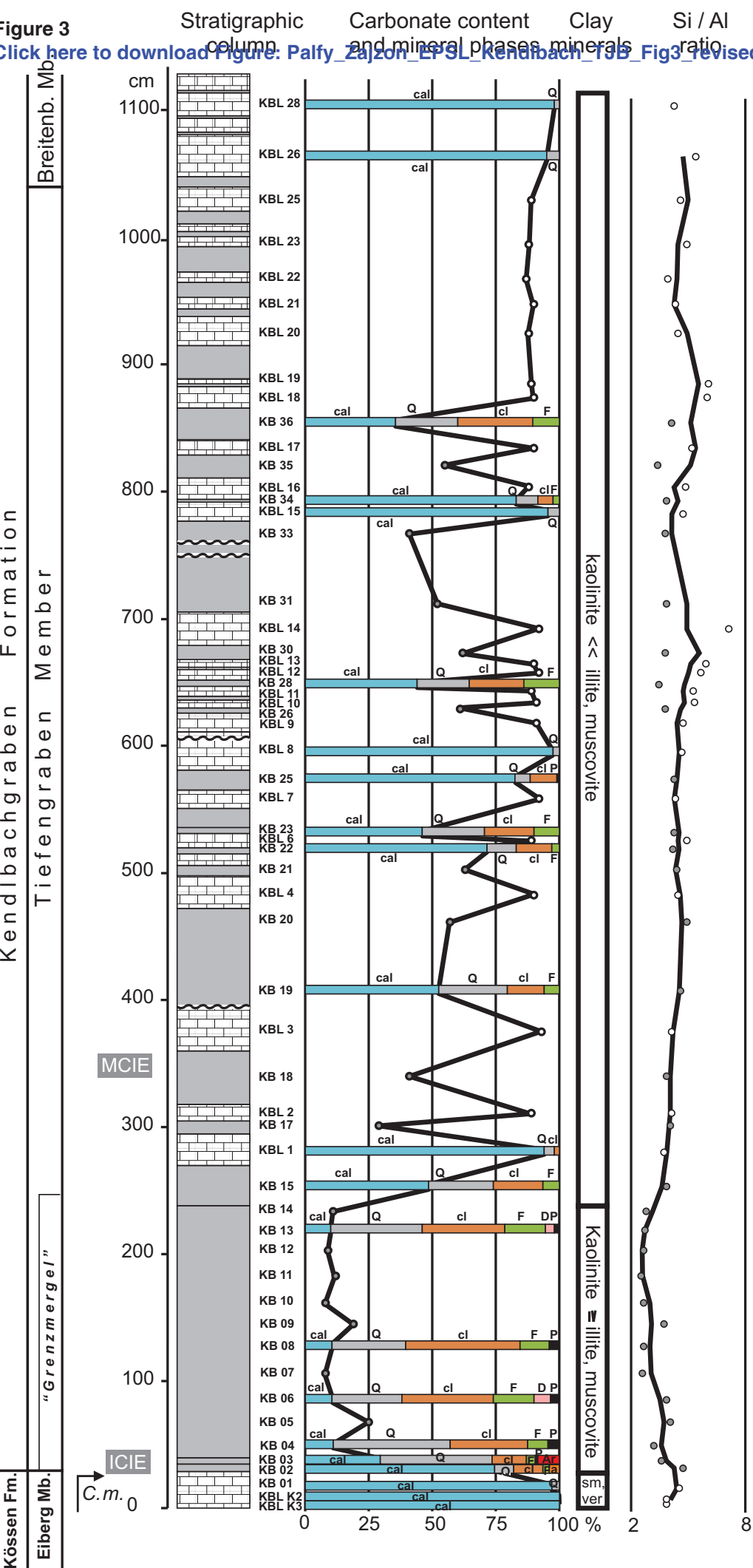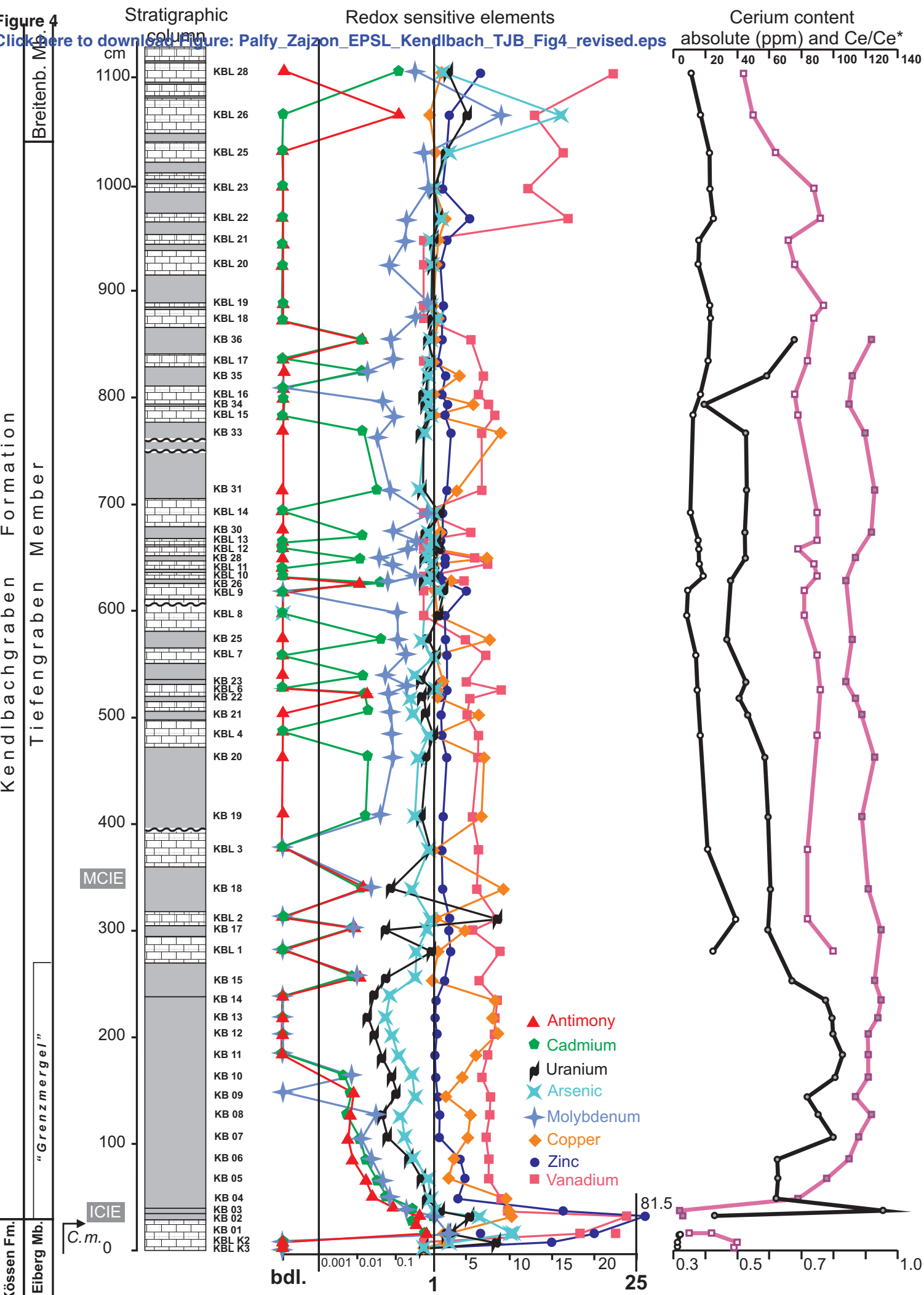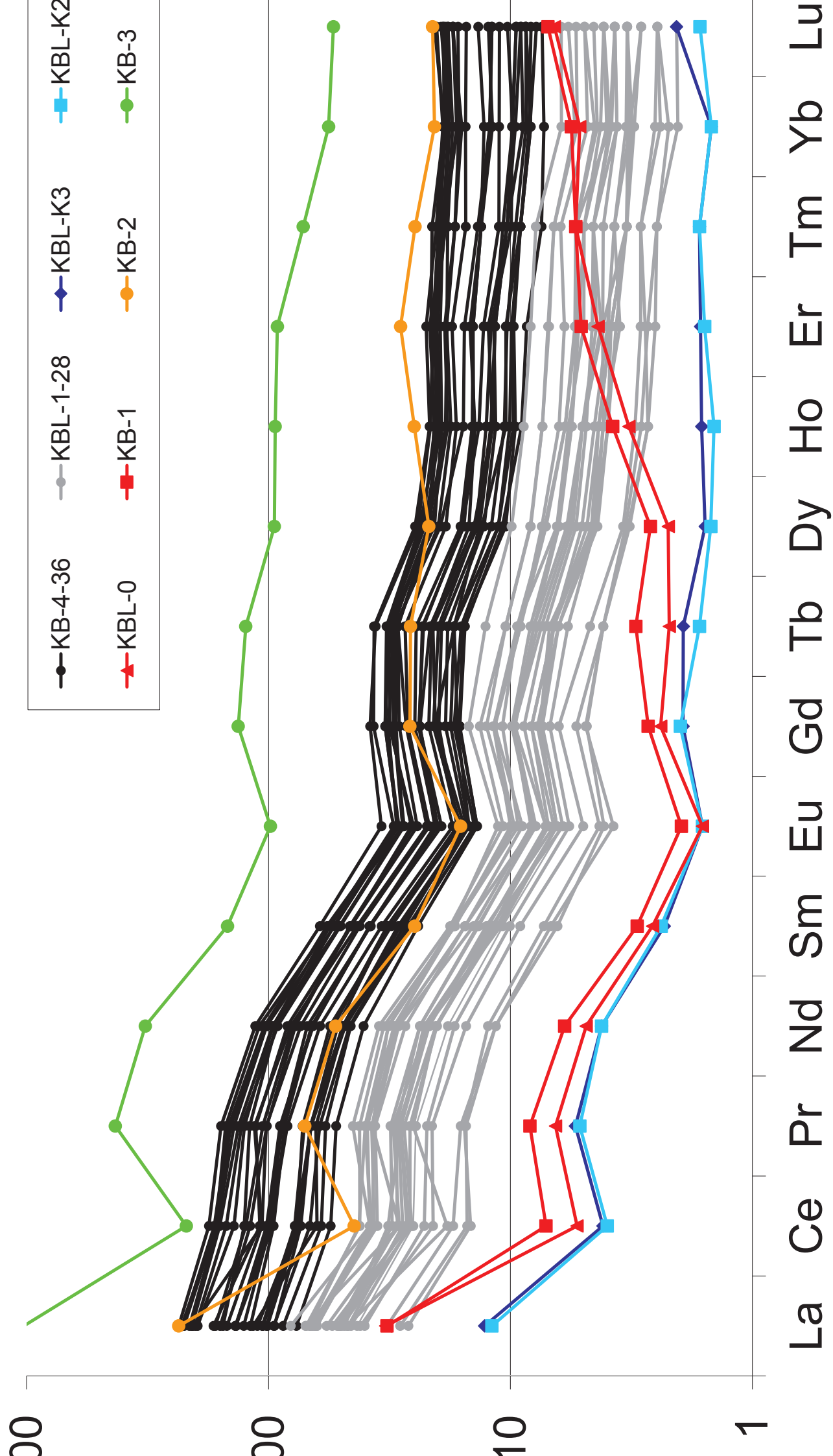
Figure 4

Figure 6
Click here to download high resolution image
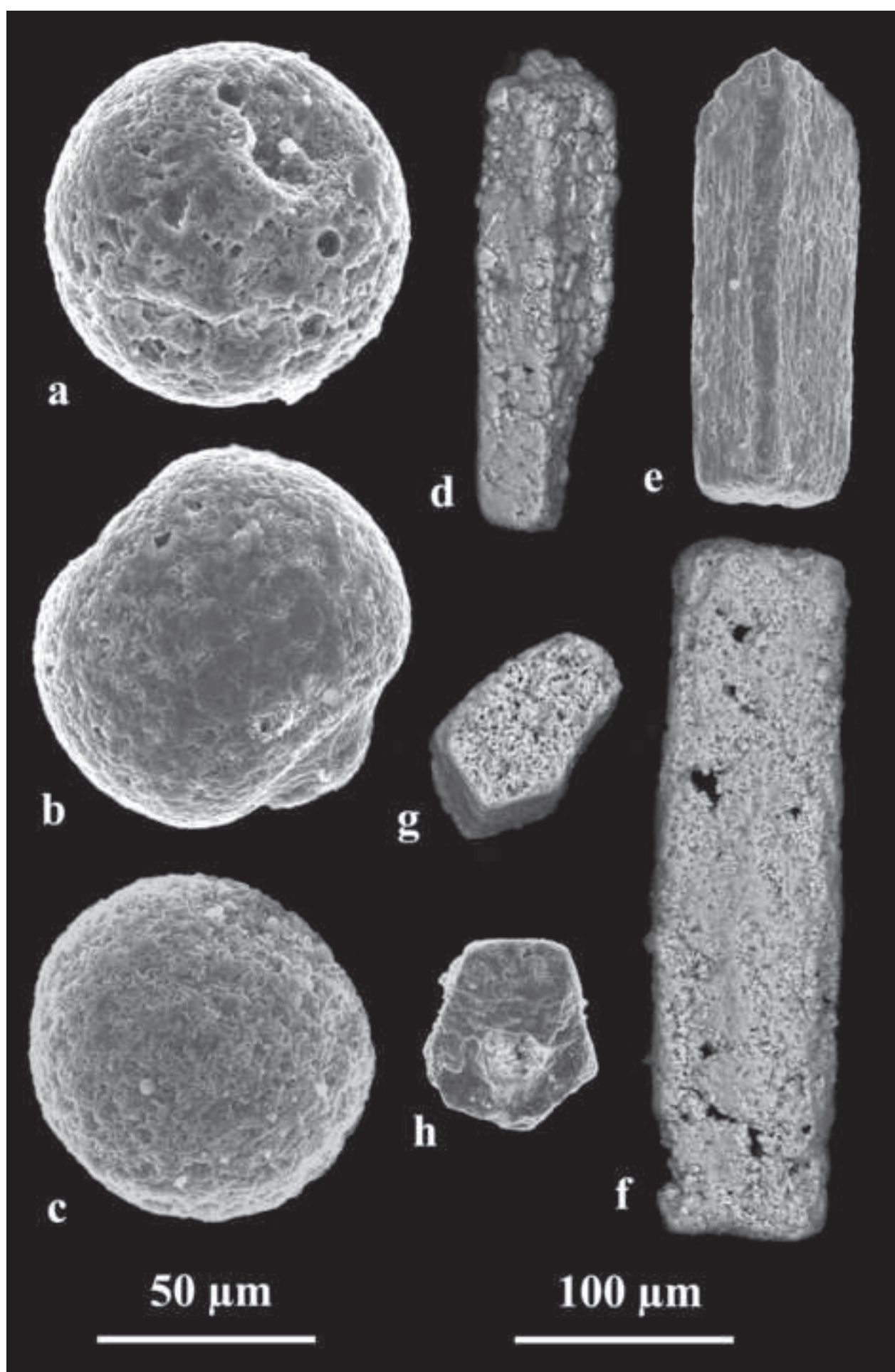
50 μm

100 μm

Sample No.↓	C	Al_2O_3	SiO_2	P_2O_5	S	CaO	Fe_2O_3	V	Cu	Zn	As	Mo	Cd	Sn	Sb	Th	U	LOI	Sum
	%	%	%	%	%	%	%	ppm	ppm	ppm	ppm	ppm	Ppm	ppm	ppm	ppm	ppm	%	%
det. limit→	0.02	0.01	0.01	0.001	0.02	0.01	0.04	8	0.1	1	0.5	0.1	0.1	1	0.1	0.2	0.1		
KBL-28	12.84	0.46	1.95	0.019	0.04	53.11	0.17	20	1.9	6	2.0	0.3	0.1	<1	<0.1	0.9	2.6	43.0	99.70
KBL-26	12.81	0.42	2.27	0.004	0.14	52.58	0.42	13	0.7	3	16.1	9.1	<0.1	<1	0.1	1.0	5.1	42.6	99.13
KBL-25	12.13	1.15	5.27	0.010	0.02	50.02	0.50	18	1.5	3	3.3	0.4	<0.1	<1	<0.1	1.1	2.8	41.5	99.54
KBL-23	11.79	1.32	6.53	0.037	0.22	49.16	0.62	22	2.2	4	2.2	1.0	<0.1	<1	<0.1	1.8	2.2	40.5	99.64
KBL-22	11.77	1.55	6.12	0.042	0.03	48.94	0.87	22	3.3	7	2.7	0.3	<0.1	<1	<0.1	1.3	2.2	41.1	100.02
KBL-21	11.98	1.23	5.33	0.014	0.03	50.43	0.50	<8	1.9	3	0.9	0.2	<0.1	<1	<0.1	1.1	1.3	41.7	100.27
KBL-20	11.93	1.37	6.16	0.032	<0.02	49.38	0.52	<8	2.2	3	1.5	0.1	<0.1	<1	<0.1	1.5	1.5	41.1	99.74
KBL-19	11.73	1.16	7.04	0.062	0.03	49.63	0.51	<8	1.4	3	1.1	0.6	<0.1	<1	<0.1	1.3	1.2	40.7	100.39
KBL-18	11.65	1.05	6.29	0.021	0.02	50.13	0.62	<8	2.4	3	2.2	0.4	<0.1	<1	<0.1	1.4	1.4	41.1	100.42
KB-36	7.16	7.00	28.72	0.050	0.20	29.49	2.88	41	9.3	16	6.0	0.5	0.1	1	0.1	7.4	3.5	28.4	99.96
KBL-17	11.67	1.25	6.51	0.012	0.04	50.13	0.51	<8	1.4	2	0.8	0.1	<0.1	<1	<0.1	1.2	1.4	41.2	100.88
KB-35	7.30	7.59	25.91	<0.001	0.10	31.00	2.21	49	9.6	18	3.9	0.1	0.1	1	<0.1	7.0	3.0	29.7	99.96
KBL-16	11.83	1.47	7.12	0.017	0.02	49.52	0.51	9	1.7	3	0.7	<0.1	<0.1	<1	<0.1	1.4	1.2	40.5	100.37
KB-34	10.14	3.20	12.39	<0.001	0.01	44.18	0.99	19	3.7	7	1.5	0.1	<0.1	1	<0.1	2.5	1.2	37.5	99.99
KBL-15	11.82	1.39	6.54	0.025	<0.02	49.88	0.41	10	1.5	3	1.0	0.1	<0.1	<1	<0.1	1.2	0.8	41.1	100.59
KB-33	5.73	9.27	35.42	0.040	0.01	23.01	3.04	49	12.4	23	2.9	0.2	0.1	2	<0.1	7.2	2.4	24.9	99.87
KB-31	7.03	7.59	29.24	0.020	0.45	28.95	2.21	45	9.1	18	2.4	0.4	0.2	1	<0.1	6.6	2.8	28.1	99.87
KBL-14	12.15	0.80	5.68	0.048	0.04	51.24	0.40	<8	1.3	2	1.1	0.5	<0.1	<1	<0.1	0.9	1.7	41.2	100.48
KB-30	8.59	5.83	22.10	0.020	0.01	34.64	2.26	37	8.9	15	3.7	0.5	0.1	1	<0.1	6.7	3.6	32.1	99.85
KBL-13	12.14	0.98	5.80	0.014	0.24	50.44	0.50	<8	1.4	2	1.1	0.3	<0.1	<1	<0.1	1.0	1.5	41.4	100.37
KBL-12	12.31	0.94	5.33	0.024	0.06	51.29	0.41	<8	1.7	2	0.6	0.2	<0.1	<1	<0.1	1.0	1.8	41.4	100.52
KB-28	6.17	9.06	31.37	0.030	0.01	25.38	3.02	52	13.4	22	4.2	0.3	0.1	2	<0.1	8.7	3.6	26.9	99.86
KBL-11	11.90	1.19	6.30	0.009	0.10	49.84	0.43	9	1.4	3	1.2	0.1	<0.1	<1	<0.1	1.2	1.3	41.1	100.11
KBL-10	12.14	1.00	5.35	0.019	0.05	50.77	0.50	<8	1.2	2	1.1	0.3	<0.1	<1	<0.1	1.1	1.4	41.4	100.20
KB-26	8.24	5.95	22.58	0.030	0.01	34.23	2.28	34	9.8	16	3.3	0.3	0.3	1	0.1	7.2	2.9	31.8	99.87
KBL-9	12.29	0.95	4.48	0.022	0.07	51.21	0.39	<8	0.8	3	1.0	<0.1	<0.1	<1	<0.1	0.6	1.4	41.7	99.91
KBL-8	12.51	0.75	3.51	0.031	0.03	51.78	0.33	<8	1.3	2	<0.5	0.1	<0.1	<1	<0.1	0.8	1.4	42.4	100.00
KB-25	10.05	3.65	15.47	<0.001	0.09	41.01	1.74	23	7.4	12	2.0	0.6	0.2	1	<0.1	4.7	3.2	35.7	99.86
KBL-7	11.89	1.12	4.85	0.009	0.14	51.32	0.38	8	1.5	3	1.0	0.2	<0.1	<1	<0.1	1.1	1.6	41.6	100.49
KB-23	8.38	5.25	22.52	0.020	0.01	35.45	2.05	31	8.3	13	1.8	0.3	0.1	1	<0.1	6.2	2.7	31.9	99.95
KBL-6	12.11	1.28	6.32	0.015	0.09	49.97	0.48	10	1.8	3	1.2	0.2	<0.1	<1	<0.1	1.1	1.1	40.6	99.98
KB-22	8.38	5.23	21.98	0.030	0.01	35.81	1.92	33	8.0	12	1.4	0.4	0.1	1	0.1	6.1	2.5	32.2	99.94
KB-21	8.13	5.11	22.61	0.030	0.01	35.50	2.09	30	8.8	12	1.5	0.4	0.1	1	<0.1	5.9	2.8	31.9	99.93
KBL-4	11.97	1.20	5.35	0.057	0.04	50.61	0.47	9	1.6	3	0.8	0.1	<0.1	<1	<0.1	1.4	1.6	41.1	100.13
KB-20	8.13	5.72	28.13	0.020	0.65	32.00	2.16	40	9.6	17	2.2	0.5	0.1	1	<0.1	6.3	3.1	28.8	99.87
KB-19	7.34	6.54	30.05	0.030	0.01	29.67	2.34	40	10.6	16	2.3	0.3	0.1	1	<0.1	7.0	2.9	28.1	99.95
KBL-3	12.01	1.17	4.87	<0.001	<0.02	51.94	0.46	9	1.6	3	0.8	<0.1	<0.1	<1	<0.1	1.4	1.1	41.4	100.80
KB-18	5.56	9.22	35.66	0.030	0.01	23.06	3.20	56	15.6	20	2.6	0.2	0.1	2	0.1	9.0	2.8	24.7	99.97
KBL-2	11.76	1.52	6.33	0.028	0.03	49.79	0.67	12	2.0	6	1.1	<0.1	<0.1	<1	<0.1	1.4	2.0	41.1	100.73
KB-17	3.95	10.88	44.26	0.050	0.02	16.27	4.00	70	17.3	36	4.8	0.1	0.1	2	0.1	12.2	2.8	19.9	99.95
KBL-1	11.39	2.15	8.00	0.015	0.03	47.87	0.81	17	3.2	6	0.9	<0.1	<0.1	<1	<0.1	1.9	1.7	40.1	100.29
reKB-15	4.15	11.00	42.46	0.070	0.03	17.39	3.87	69	11.3	28	5.2	0.1	0.2	2	0.1	9.2	3.8	20.5	99.96
KB-15	4.21	11.03	42.31	0.090	0.03	17.50	3.95	74	11.3	28	4.6	0.1	0.1	2	<0.1	11.4	4.0	20.4	99.94
KB-14	1.58	18.07	50.25	0.070	0.02	6.17	3.71	113	22.0	19	1.1	<0.1	<0.1	3	<0.1	13.1	2.1	14.8	99.85
KB-13	1.44	18.76	50.87	0.050	0.01	5.86	3.52	117	22.6	19	1.0	<0.1	<0.1	4	<0.1	14.2	2.0	14.2	99.97
KB-12	1.31	19.18	50.83	0.060	0.02	5.08	4.08	122	25.1	23	1.3	<0.1	<0.1	4	<0.1	14.7	2.7	14.0	99.96
KB-11	1.60	19.26	48.46	0.050	0.04	6.67	3.83	120	23.8	21	1.9	0.1	<0.1	4	<0.1	16.0	2.3	15.3	99.97
KB-10	1.13	19.09	51.44	0.070	0.03	4.50	4.29	116	23.8	24	3.9	0.1	0.1	4	<0.1	17.0	2.4	14.0	99.96
KB-9	2.67	13.78	51.16	0.080	0.01	10.44	3.27	98	16.7	21	3.8	<0.1	0.1	3	0.1	12.5	2.6	15.5	99.96
KB-8	0.97	19.33	52.18	0.060	0.52	3.75	5.78	124	23.1	30	1.9	0.4	0.1	4	0.1	16.0	3.1	12.8	99.84
KB-7	1.15	19.46	51.23	0.050	0.51	4.63	4.62	120	23.2	30	2.6	0.2	0.2	4	0.1	16.4	3.1	13.6	99.82
KB-6	3.34	12.33	47.70	0.060	0.45	12.12	3.49	88	15.6	49	3.0	0.3	0.2	3	0.1	11.5	2.3	17.3	99.83
KB-5	3.82	11.74	47.49	0.060	0.76	13.78	3.95	96	17.0	61	6.6	0.5	0.4	3	0.2	12.6	3.2	17.4	99.97
KB-4	3.04	15.88	51.30	0.060	0.67	7.31	5.29	138	29.3	61	12.9	1.0	0.7	4	0.4	15.2	5.2	15.1	99.94
KB-3	7.42	6.22	22.39	2.720	0.03	33.48	3.14	64	16.0	90	8.1	1.4	1.1	2	0.6	6.5	12.6	29.4	99.74

KB-2	12.81	1.48	7.05	1.190	0.04	46.42	2.78	30	13.4	106	8.5	1.6	1.4	<1	0.8	1.3	7.0	39.5	99.80
KB-1	12.81	0.58	2.62	0.030	<0.01	53.06	1.09	11	1.4	4	6.1	1.7	0.1	<1	0.2	0.6	1.6	41.7	99.87
KBL-0	12.62	0.37	2.50	0.040	0.03	52.90	1.36	9	1.2	8	4.2	1.2	0.2	<1	0.3	0.4	1.3	42.4	100.30
KBL-K2	12.92	0.15	0.58	0.008	0.02	55.23	0.07	<8	0.5	3	0.6	<0.1	<0.1	<1	<0.1	0.2	1.7	43.2	100.00
KBL-K3	13.06	0.09	0.35	0.018	0.02	56.23	0.07	<8	0.2	5	0.6	0.1	0.2	<1	<0.1	<0.2	2.0	43.2	100.52

Sample No.↓	La	Ce	Pr	Nd	Sm	Eu	Gd	Tb	Dy	Ho	Er	Tm	Yb	Lu
det. limit→	0.1	0.1	0.02	0.3	0.05	0.02	0.05	0.01	0.05	0.02	0.03	0.01	0.05	0.01
KBL-28	11.1	11.0	2.25	9.2	1.73	0.40	1.88	0.29	1.53	0.31	0.84	0.13	0.63	0.10
KBL-26	16.5	17.4	3.31	14.5	2.55	0.63	2.92	0.46	2.40	0.49	1.31	0.19	1.00	0.15
KBL-25	19.0	23.0	3.99	15.8	2.61	0.60	2.63	0.38	2.01	0.41	1.11	0.16	0.86	0.13
KBL-23	14.8	22.7	3.56	14.4	2.52	0.54	2.31	0.34	1.75	0.33	0.85	0.13	0.71	0.11
KBL-22	16.4	25.3	3.75	15.1	2.49	0.56	2.31	0.33	1.73	0.33	0.86	0.13	0.73	0.12
KBL-21	12.8	15.9	2.52	10.3	1.76	0.34	1.45	0.23	1.06	0.22	0.61	0.08	0.50	0.07
KBL-20	11.7	15.4	2.45	9.2	1.65	0.36	1.52	0.23	1.11	0.23	0.56	0.09	0.52	0.07
KBL-19	14.8	22.5	3.26	13.1	2.09	0.46	1.91	0.28	1.38	0.28	0.67	0.11	0.63	0.09
KBL-18	15.4	23.0	3.48	13.7	2.51	0.52	2.12	0.34	1.56	0.32	0.79	0.12	0.65	0.10
KB-36	36.2	76.0	10.66	42.1	7.88	1.65	6.30	1.09	4.72	0.87	2.46	0.33	1.98	0.29
KBL-17	15.1	21.4	3.23	12.3	2.27	0.45	1.90	0.27	1.34	0.28	0.66	0.10	0.59	0.09
KB-35	32.0	58.1	7.94	29.6	5.63	1.12	4.65	0.78	3.43	0.66	1.96	0.25	1.59	0.25
KBL-16	13.5	17.4	2.72	10.0	1.74	0.39	1.61	0.24	1.17	0.24	0.61	0.08	0.53	0.08
KB-34	11.4	19.3	2.54	10.0	1.61	0.36	1.48	0.25	1.08	0.23	0.66	0.08	0.51	0.08
KBL-15	9.8	12.6	1.88	6.9	1.34	0.28	1.24	0.17	0.83	0.17	0.46	0.07	0.41	0.06
KB-33	23.7	45.2	5.94	21.8	3.91	0.77	3.20	0.57	2.54	0.53	1.54	0.22	1.36	0.20
KB-31	23.9	46.5	5.94	22.3	4.19	0.83	3.26	0.62	2.72	0.56	1.57	0.22	1.34	0.21
KBL-14	7.6	10.4	1.43	5.2	1.00	0.21	0.96	0.15	0.79	0.15	0.44	0.07	0.39	0.06
KB-30	22.2	44.4	5.96	23.4	4.72	0.93	3.89	0.70	3.18	0.58	1.66	0.22	1.34	0.21
KBL-13	10.7	15.7	2.32	9.1	1.68	0.36	1.48	0.24	1.12	0.24	0.61	0.08	0.53	0.08
KBL-12	12.0	16.2	2.53	9.8	1.82	0.40	1.73	0.26	1.30	0.27	0.73	0.11	0.62	0.09
KB-28	24.8	44.8	5.99	22.3	4.28	0.85	3.65	0.66	3.12	0.64	1.86	0.26	1.59	0.23
KBL-11	11.0	16.8	2.59	9.8	1.85	0.37	1.61	0.24	1.23	0.25	0.63	0.09	0.54	0.08
KBL-10	12.2	18.6	2.79	10.7	2.01	0.44	1.90	0.29	1.42	0.28	0.70	0.11	0.59	0.09
KB-26	20.4	36.5	5.18	20.7	3.76	0.79	3.36	0.58	2.72	0.54	1.56	0.22	1.35	0.19
KBL-9	6.7	9.1	1.36	5.2	0.94	0.23	0.95	0.15	0.81	0.16	0.43	0.06	0.36	0.06
KBL-8	6.2	8.8	1.38	5.6	1.07	0.24	1.05	0.15	0.78	0.15	0.40	0.06	0.33	0.05
KB-25	18.0	33.4	4.68	18.3	3.54	0.77	3.18	0.56	2.62	0.50	1.36	0.18	1.18	0.18
KBL-7	9.4	13.7	1.97	7.7	1.48	0.32	1.35	0.21	1.08	0.22	0.58	0.08	0.52	0.08
KB-23	26.1	45.9	6.44	25.2	4.57	0.90	4.09	0.72	3.36	0.70	1.91	0.24	1.60	0.23
KBL-6	10.1	15.2	2.19	8.2	1.58	0.34	1.45	0.23	1.08	0.24	0.62	0.09	0.52	0.07
KB-22	22.3	40.7	5.48	20.9	3.87	0.83	3.47	0.62	2.91	0.59	1.64	0.23	1.40	0.21
KB-21	24.9	47.0	6.33	24.4	4.75	0.92	4.02	0.76	3.32	0.67	1.84	0.25	1.55	0.22
KBL-4	11.9	17.7	2.64	10.7	1.99	0.45	1.94	0.30	1.55	0.31	0.83	0.12	0.69	0.10
KB-20	27.9	57.5	7.64	30.0	5.59	1.15	4.70	0.83	3.84	0.75	2.05	0.27	1.81	0.27
KB-19	32.2	59.9	7.84	31.3	5.56	1.14	4.89	0.89	3.90	0.80	2.27	0.32	1.98	0.29
KBL-3	15.7	22.0	3.34	13.4	2.26	0.50	2.28	0.33	1.80	0.35	0.95	0.15	0.78	0.12
KB-18	32.0	61.5	7.99	29.9	5.59	1.08	4.67	0.84	3.78	0.79	2.27	0.32	1.93	0.30
KBL-2	27.2	38.0	5.68	22.1	4.04	0.87	4.02	0.62	3.26	0.66	1.84	0.25	1.44	0.22
KB-17	29.7	59.3	7.44	27.7	5.01	0.97	4.27	0.77	3.60	0.78	2.33	0.32	2.09	0.33
KBL-1	15.9	25.5	3.55	13.6	2.55	0.54	2.47	0.38	2.00	0.41	1.10	0.16	0.88	0.14
reKB-15	37.2	71.9	9.06	35.0	6.79	1.41	6.21	1.11	5.28	1.11	3.25	0.45	2.71	0.42
KB-15	38.9	74.9	9.42	35.8	6.69	1.44	6.17	1.16	5.61	1.14	3.43	0.45	2.91	0.44
KB-14	48.7	95.9	11.85	43.5	7.48	1.56	5.84	1.08	4.82	0.98	2.92	0.41	2.65	0.40
KB-13	49.8	98.0	12.37	46.1	7.85	1.63	6.47	1.17	5.00	1.07	3.10	0.46	2.68	0.42
KB-12	52.4	99.2	12.77	46.1	8.43	1.62	6.45	1.16	5.49	1.08	3.20	0.46	2.93	0.47
KB-11	55.2	106.3	14.00	51.3	9.02	1.91	7.47	1.31	5.84	1.19	3.32	0.48	3.00	0.46
KB-10	53.1	101.1	13.03	47.1	8.34	1.63	6.47	1.18	5.74	1.10	3.23	0.47	3.05	0.46
KB-9	46.1	83.9	11.21	43.3	8.21	1.70	7.23	1.33	6.01	1.20	3.54	0.49	3.09	0.49
KB-8	47.1	90.2	11.53	41.5	7.41	1.54	5.95	1.13	5.27	1.12	3.28	0.45	2.93	0.45
KB-7	53.7	99.4	13.41	49.4	8.22	1.56	5.96	1.11	5.30	1.03	2.91	0.44	2.82	0.44
KB-6	34.9	64.2	9.11	33.3	6.17	1.21	5.22	0.99	4.49	0.93	2.77	0.37	2.49	0.37
KB-5	39.6	65.6	10.07	37.8	6.72	1.36	5.67	1.06	5.14	1.01	2.97	0.41	2.58	0.42
KB-4	48.3	64.3	10.18	36.6	6.33	1.24	5.30	1.06	5.22	1.15	3.38	0.51	3.05	0.50
KB-3	241.5	131.9	38.32	146.2	21.73	5.50	26.25	4.51	22.97	5.22	14.60	1.74	9.17	1.31
KB-2	55.2	26.7	6.31	23.9	3.66	0.90	5.12	0.94	5.28	1.39	4.52	0.60	3.35	0.51

KB-1	7.6	4.3	0.74	2.7	0.44	0.11	0.53	0.11	0.64	0.21	0.81	0.13	0.91	0.17
KBL-0	7.7	3.2	0.58	2.2	0.38	0.09	0.47	0.08	0.54	0.18	0.69	0.13	0.84	0.16
KBL-K2	2.8	2.4	0.46	1.9	0.35	0.09	0.39	0.06	0.36	0.08	0.25	0.04	0.24	0.04
KBL-K3	3.0	2.5	0.48	1.9	0.34	0.09	0.38	0.07	0.38	0.09	0.26	0.04	0.24	0.05

Table 3
Click here to download Table: Palfy_Zajzon_EPSL_Kendlbach_TJB_Table_3.doc

	calcite	quartz	illite/ muscovite	kaolinite	smectite	albite	sanidine	microcline	pyrite	gypsum	dolomite	aragonite	apatite-F
KBL-28	97.8	2.2											
KBL-26	95.2	4.8											
KB-36	35.7	24.3	22.4	5.4	1.5	5.0	5.7						
KB-34	82.8	8.9	3.1	2.1	0.4		2.6						
KBL-15	95.5	4.3			0.3								
KB-28	44.2	20.1	14.2	5.9	1.4	5.0	9.1						
KBL-8	97.3	2.7											
KB-25	82.7	5.8	7.9	2.1	0.5				1.1				
KB-23	45.9	24.5	12.8	5.6	1.0	5.7	4.6						
KB-22	71.4	11.7	11.2	2.0	0.9		2.7						
KB-19	52.4	27.1	10.6	3.5	0.4	5.8							
KBL-1	93.8	3.6	2.5		0.1								
KB-15	48.3	25.8	11.9	5.7	1.9	4.0		2.3					
KB-13	10.0	35.9	16.8	14.4	1.6	8.7		7.1	1.4	0.8	3.5		
KB-8	10.3	29.0	19.3	24.1	1.8			11.5	3.9				
KB-6	9.9	28.1	22.8	12.2	0.9	9.2	6.7		3.3	0.5	6.5		
KB-4	10.8	46.3	12.0	17.8	0.6	8.1			3.4	0.9			
KB-3	29.5	44.1	6.1	6.8	0.5	3.7			0.8			8.4	
KB-2	74.7	7.3	8.3	2.7	0.1	2.4							4.1
KB-1	96.8	3.2											
KBL-K2	100.0												
KBL-K3	100,0												